Molecular dynamics study of novel cryoprotectants and of CO_2 capture by sI clathrate hydrates

Michael Nohra

Thesis submitted to the

Faculty of Graduate and Postdoctoral Studies

In partial fulfillment of the requirements

For the MSc degree in Chemistry

Department of Chemistry

Faculty of Science

University of Ottawa

Table of Contents

Table of Contents……..ii

Abstract……iii

List of Figures……..iv

List of Tables……...vi

List of Equations……..…vii

List of Abbreviations……...…ix

Acknowledgements……..….x

Chapter 1: Introduction and applications of molecular dynamics simulations

General introduction……...……..…1

Chapter 2: Investigating ice recrystallization inhibition activity of novel cryprotectants

Introduction……...7

Methodology……21

Computational details……...……..27

Results and discussion…….32

Conclusion……...40

Chapter 3: Investigating the feasibility of sI clathrate hydrates as carbon capture tools

Introduction……46

Methodology……...……58

Computational details……...……..…70

Results and discussion…….77

Conclusion……..……94

Chapter 4: Future investigations and applications

Conclusions and future work……102

Abstract

The first project in this work used classical molecular dynamics to study the ice recrystallization inhibition potential of a series of carbohydrates and alcochols, using the hydration index, partial molar volumes and isothermal compressibilities as parameters for measuring their cryogenic efficacy. Unfortunately, after 8 months of testing, this work demonstrates that the accuracy and precision of the density extracted from simulations is not sufficient in providing accurate partial molar volumes. As a result, this work clearly demonstrates that current classical molecular dynamics technology cannot probe the volumetric properties of interest with sufficient accuracy to aid in the research and development of novel cryoprotectants.

The second project in this work used molecular dynamics simulations to evaluate the Gibbs free energy change of substituting CO_2 in sI clathrate hydrates by N_2,CH_4, SO_2 and H_2S flue gas impurities under conditions proposed for CO_2 capture (273 K, 10 bar). Our results demonstrate that CO_2 substitutions by N_2 in the small sI cages were thermodynamically favored. This substitution is problematic in terms of efficient CO_2 capture, since the small cages make up 25% of the sI clathrate cages, therefore a significant amount of energy could be spent on removing N_2 from the flue gas rather than CO_2. The thermodynamics of CO_2 substitution by CH_4, SO_2 and H_2S in sI clathrate hydrates was also examined. The substitution of CO_2 by these gases in both the small and large cages were determined to be favorable. This suggests that these gases may also disrupt the CO_2 capture by sI clathrate hydrates if they are present in large concentrations in the combustion flue stream. Similar substitution thermodynamics at 200 K and 10 bar were also studied. With one exception, we found that the substitution free energies do not significantly change and do not alter the sign of thermodynamics. Thus, using a lower capture temperature does not significantly change the substitution free energies and their implications for CO_2 capture by sI clathrate hydrates.

List of Figures

Figure 1.1: General structure of a naturally occurring AFGPs..……. 2

Figure 1.2: Close-up the small and large cages in sI clathate hydrate……..……4

Figure 2.1: Structure of native AFGP-8 from *Gagus Ogac*…….. 11

Figure 2.2: Schematic representation of the quasi-liquid layers……... 13

Figure 2.3: IRI activity of native AFGP-8 and some of its analogues…….. 14

Figure 2.4: IRI activity of various monosaccharides and Disaccharides as a function of the hydration number…….…….. 15

Figure 2.5: IRI activity of various monosaccharides and disaccharides as a function of the hydration index……...……... 16

Figure 2.6: AFGP-8 analogue; Schematic representation of the hydroxyl groups participating in hydrogen bonding in a AFGP-8 analogue…….… 18

Figure 2.7: Molecular dynamics snapshots of the conformations for 4 different AFGP analogues...…….. 19

Figure 2.8: Test structures of carbohydrates studied in this work……. 20

Figure 2.9: Isothermal and adiabatic compressibilities behavior of water at different temperratures……. ……....24

Figure 2.10: Snapshot of a simulation cell of a solvated carbohydrate used in this work……..27

Figure 2.11: Density error analysis for all alcohols…….. 35

Figure 2.12: Simulated partial molar volume of propanol at different concentrations…….. 36

Figure 2.13: Simulation cell snapshot illustrating propanol interactions at the MD detection limit…… 38

Figure 3.1: SiO_2, silicate structure (zeolite)……..……. 49

Figure 3.2: Clathrate hydrate hydrogen bonding network……. 50

Figure 3.3: Proposed clathrate hydrate apparatus for CO_2 recovery……. 51

Figure 3.4: Pressure and temperature conditions for hydrate formation……... 52

Figure 3.5: Example of carbon dioxide deep sea storage using clathrate hydrates……... 53

Figure 3.6: Ocean floor offering favorable conditions for clathrate formation……. 53

Figure 3.7: Clathrate hydrate reservoir found under the permafrost……. 54

Figure 3.8: The structures of small and large cages in sI clathrate hydrate……... 55

Figure 3.9: Snapshot of $CO_2 \rightarrow SO_2$ transformation using thermodynamic integration in this study……... 65

Figure 3.10: Free energy behavior for different λ values of the $CO_2 \rightarrow SO_2$ substitution……. 72

List of Tables

Table 2.1: Comparison of theoretical and simulated partial molar volumes for the carbohydrates used in this work…….. 32

Table 2.2: Comparison of theoretical and simulated partial molar volumes for the alcohols used in this work ……..…….……... 34

Table 2.3: Partial molar volume of propanol at different simulated concentrations……. 37

Table 3.1: List of atomic point charges and Lennard-Jones parameters for the molecules used in this work……..... 71

Table 3.2: Gibbs free energy of CO_2(clathrate) → CH_4(clathrate) substitutions at 273 K and 10 bar…….. 78

Table 3.3: Gibbs free energy of CO_2(clathrate) → N_2(clathrate) substitutions at 273 K and 10 bar……..… 81

Table 3.4: Thermophysical data and residual contributions to the Gibbs free energy for the molecules used in this study…….. 83

Table 3.5: Simulation cell volumes ($Å^3$) for each clathrate used in this study…….……... 84

Table 3.6: Van der Waals radii (Å) and polarity for guest species used in this work…….…… 84

Table 3.7: Gibbs free energy of CO_2(clathrate) → SO_2(clathrate) substitutions at 273 K and 10 bar…….. 85

Table 3.8: Gibbs free energy of CO_2(clathrate) → H_2S(clathrate) substitutions at 273 K and 10 bar…….. 87

Table 3.9: Gibbs free energy of CO_2(clathrate) → Y(clathrate) substitutions at 200 K and 10 bar…….. 90

List of Equations

Equation 2.1: Hydration index…… 21

Equation 2.2: Partial molar volume…… 21

Equation 2.3: Molality…….. 21

Equation 2.4: Hydration number……..... 22

Equation 2.5: Mole fraction…….. 22

Equation 2.6: Isentropic compressibility…….. 23

Equation 2.7: Isentropic-Isothermal compressibility approximation……..…….... 23

Equation 2.8: Isothermal compressibility via fluctuation method…… 25

Equation 2.9: Isothermal compressibility via finite difference method…… 25

Equation 2.10: Density required in the first simulation

of the finite difference method……... 26

Equation 2.11: Density required in the second simulation

of the finite difference method…….. 26

Equation 3.1: Phase 1 reaction of CO_2 capture via liquid amine sorbent……. 47

Equation 3.2: Phase 2 reaction of CO_2 capture via liquid amine sorbent……. 47

Equation 3.3: Intra and intermolecular interaction potential energy function…….. 59

Equation 3.4: Non-bonded potential energy function……... 59

Equation 3.5: Electrostatic potential……. 59

Equation 3.6: Van der Waals potential……. 60

Equation 3.7: Linear Kirkwood coupling parameter method……... 60

Equation 3.8: Gibbs free energy via thermodynamic integration……. 61

Equation 3.9: Non-linear Kirkwood coupling parameter method……. 62

Equation 3.10: General CO_2 sI clathrate substitution reaction with impurity guest Y……. 63

Equation 3.11: CO_2 substitution reaction in the clathrate hydrate phase with guest Y…..... 63

Equation 3.12: Error function mixing function……. 65

Equation 3.13: Polynomial function mixing function……... 65

Equation 3.14: Trigonometric function mixing function…….. 65

Equation 3.15: Y gas substitution reaction with CO_2 in the gas phase……...….. 66

Equation 3.16: Non-ideality free energy contribution for CO_2..... 66

Equation 3.17: Residual chemical potential component of the non-ideal contribution..…... 67

Equation 3.18: Total Gibbs free energy for CO_2→Y guest substitution……..…… 67

Equation 3.19: First ideal gas approximation……... 68

Equation 3.20: Second ideal gas approximation……... 68

Equation 3.21: Clathrate incompressibility approximation…….. 68

Equation 3.22: Total Gibbs free energy approximation…… 68

Equation 3.23: Full non-bonded potential…… 68

Equation 3.24: Partial non-bonded potential (no charge contribution)……. 69

Equation 3.25: Lorentz Bertholet combination rules for ε…… 74

Equation 3.26: Lorentz Bertholet combination rules for σ……... 74

Equation 3.27: All cage sI clathrate substitution reaction CO_2→CH_4……..… 78

Equation 3.28: Large cage sI clathrate substitution reaction CO_2→CH_4 ……..…….. 78

Equation 3.29: Small cage sI clathrate substitution reaction CO_2→CH_4 ……..…….. 79

Equation 3.30: All cage sI clathrate substitution reaction CO_2→N_2 ……... 80

Equation 3.31: Large cage sI clathrate substitution reaction CO_2→ N_2……...…… 81

Equation 3.32: Small cage sI clathrate substitution reaction CO_2→ N_2 ……..…… 81

Equation 3.33: All cage sI clathrate substitution reaction CO_2→SO_2…..……... 85

Equation 3.34: Large cage sI clathrate substitution reaction CO_2→ SO_2……. 85

Equation 3.35: Small cage sI clathrate substitution reaction CO_2→ SO_2……. 85

Equation 3.36: All cage sI clathrate substitution CO_2→H_2S……....…….... 87

Equation 3.37: Large cage sI clathrate substitution CO_2→ H_2S……..……. 88

Equation 3.38: Small cage sI clathrate substitution CO_2→ H_2S ……. 88

List of Abbreviations

AFGP: Antifreeze glycoprotein

AM1-BCC: Austin model 1- bond charge correction

CCS: Carbon capture and storage

DMSO: Dimethyl sulfoxide

Elec: Electrostatics

GAFF: Generalized amber force field

GHG: Greenhouse gas

IR: Infrared radiation

IRI: Ice recrystallization inhibition

IRMOF: Isoreticular metal organic framework

MD: Molecular dynamics

MOF: Metal organic framework

NTP: Constant number of particles, temperature and pressure

NVT: Constant number of particles, volume and temperature

PMV: Partial molar volume

QLL: Quasi-liquid layer

QSAR: Qualitative structure-activity relation

RESP: Restrained electrostatic potential

S and L: Small cage in sI clathrate and large cage in sI clathrate

sH clathrate hydrate: Structure H clathrate hydrate

sI clathrate hydrate: Structure I clathrate hydrate

sII clathrate hydrate: Structure II clathrate hydrate

TI: Thermodynamic integration

TOT: Total

TRAPPE: Transferable potential for phase equilibira

VdW: Van der Waals

ZIF: Zeolitic imidazolate framework

Acknowledgements

First I would like to thank my supervisor Professor Tom Woo for giving me the opportunity to explore computational research; I would like thank him for allowing me to pursue my Master's degree in Chemistry. I would also like to thank him for his insights and help during the course my studies and on this thesis, without his guidance I would have never accomplished what I did. I want to give a special thanks to Saman Alavi for his help and support, and all the insightful discussions we have had throughout my degree. Also, I want to thank him for his help and co-authorship with my first publication. I would also like to thank the rest of the Woo Lab for a great experience. Especially, Nick Trefiak who was always there during my undergraduate studies. I would also like to thank Peter Boyd, and Arif Ismail for making the workplace enjoyable. Their friendship and support was important. Finally, I would like to thank my family. My mom, for her constant support, and encouragement. My brother who has always supported me and my dad for always believing in me. Most importantly I would like to thank my incredible wife for her constant support. I want to thank her most of all for her patience during my graduate studies, especially during the writing of my thesis. I would like to thank her as well for ensuring my success. Without her I could have never completed my studies.

Chapter 1: Introduction and applications of molecular dynamics simulations

General introduction

Classical molecular dynamics (MD) calculations involve simulating the nuclear motion of a molecule or material using Newtonian or classical equations of motion (i.e. F=ma).[1] These simulations have developed into a powerful tool to examine the temporal evolution of systems at the atomic scale.[1] For example, they are often used to examine the dynamics of protein folding processes.[2] In these simulations, the forces acting on the nuclei are determined from highly parameterized empirical potentials or so-called molecular mechanics force fields.[1] The efficiency of the force field calculations has allowed for simulations of systems containing hundreds of thousands of atoms for several nanoseconds to be common place.[2] For example, Levy et al. recently explored the mediation effect of water on protein folding.[3] New insights on the dynamics of protein folding/unfolding (micro to millisecond time scale) of various viral strains such as the bovine papilloma virus were observed in the presence of water. This lead to a more fundamental understanding of the mechanism of action in this biological process.[3] Classical molecular dynamics simulations are also often used to examine the free energy barriers of processes, through both physical and unphysical pathways.[1] For example, Roux et al. have used this methodology to examine the free energy profile of ions passing through a cell membrane. In this process, sodium ions are transmutated (transformed) into potassium ions at various positions in the ion channel resulting in better insight on the selectivity gradient along the channel.[4]

In this thesis, classical molecular dynamics simulations were utilized in two distinct projects. The first project used classical molecular dynamics to study the ice recrystallization

inhibition potential of a series of glycoproteins developed in the Ben lab at the University of Ottawa. In the second project, molecular dynamics simulations were used to evaluate the free energies of CO_2 capture by clathrate hydrates in the presence of common combustion gas impurities.

The first part of the thesis work (Chapter 2) involves the study of antifreeze glycoproteins (AFGPs) and various synthetic analogues developed by the Ben lab for cryopreserving organs and tissue. AFGPs typically consist of a repeating (Ala-Ala-Thr) polypeptide backbone and a variety of carbohydrates bound to a hydroxyl oxygen on the amino acid residues located in the backbone.[5] Figure 1.1 depicts the general structure of a naturally occurring AFGP.[5]

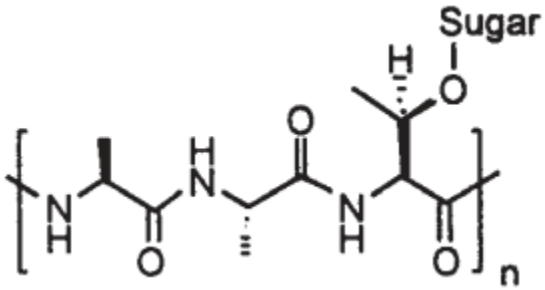

Figure 1.1: General structure of a naturally occurring AFGP. *n* represents the number of repeating subunits and sugar can represent any carbohydrate (i.e. galactose, sucrose etc…) Reproduced from reference [5][5]

Ben and coworkers empirically developed a so-called hydration index that could be correlated with the cryogenic performance of the glycoproteins.[6] The hydration index was a parameter based on the hydration number per molar volume of the compound in question.[7] In collaboration with the Ben lab, molecular dynamics simulations were performed on the AFGPs by former Woo lab members.[8] From these simulations, it was suggested that the hydroxyl-hydroxyl hydrogen bonding found in the carbohydrate moiety of the AFGP and

distances between the carbohydrate moiety and the polypeptide backbone presented a direct correlation to cryogenic performance for the available set of AFGP analogues.[8] More recently, I performed MD simulations on a larger test set of AFGP analogues synthesized in the Ben lab and found that the correlation broke down on this larger data set. Thus, the objective of this first project was to investigate whether molecular dynamics simulations could be used to directly evaluate the hydration index developed by the Ben lab. If the hydration index could be predicted from molecular dynamics simulations, such simulations could be used to screen for new AFGP analogues. This would be extremely valuable to the development of new AFGP's as their synthesis is very time consuming and having a screening tool would help focus labour intensive lab efforts. Unfortunately, after approximately 8 months of testing, it was concluded that molecular dynamics simulations could not be used to calculate the hydration index with enough accuracy to yield predictive results. Thus, this project was abandoned and a second project that was more aligned with the Woo lab's interests in CO_2 capture and storage was pursued.

In the third chapter of this thesis, classical molecular dynamics simulations were used to examine clathrate hydrate formation as a means of capturing CO_2 from coal combustion exhaust gases. Under pressure, water is known to form ice-like cages around small non-polar molecules such as CO_2 called clathrate hydrates as shown in figure 1.2.[9]

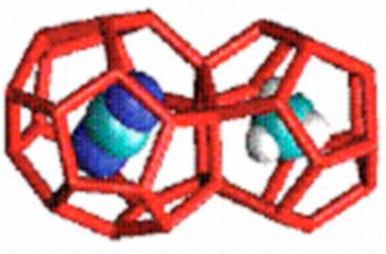

Figure 1.2: Close-up of a sI clathate hydrate. Small cage is occupied with the CH_4 guest and large cage with a CO_2 guest. The oxygen atoms of the clathrate water framework are connected by solid red lines, and the hydrogen atoms omitted for clarity. Reproduced from reference [10][10]

It has recently been proposed to use clathrate hydrates as a means of capturing post-combustion CO_2 by bubbling the exhaust gas through water under pressure.[11,12] If CO_2 clathrate hydrates preferentially form over other gases, such as N_2, then this could be used as a means of removing CO_2 from combustion gases for subsequent permanent storage. For example, once clathrate hydrates are saturated with CO_2 captured from the flue stream in coal combustion plants, it can subsequently be removed as a solid and transported for permanent storage to locations that promote favorable hydrate formation (i.e. under ocean beds). The objectives of this project were to use molecular dynamics simulations to examine the thermodynamic preference of CO_2 clathrate hydrate formation compared to other combustion flue gases such as SO_2, CH_4, N_2, and H_2S. If there is a strong thermodynamic driving force to form clathrate hydrates with gases other than CO_2, this may disrupt the CO_2 capture process or minimally make it less efficient. Molecular dynamics simulations combined with transmutation based thermodynamic integration methods were used to examine the relative free energies of clathrate hydrates containing these aforementioned gases (both pure and mixtures). The free energies were dissected into separate, electrostatic and Van der Waals components for further analysis. This work has been published in the Journal of Chemical Thermodynamics as an invited article. Nohra, M.; Woo, T.K.; Alavi, S.;

Ripmeester, J.A. "Molecular dynamics free energy calculations for CO_2 capture in structure I clathrate hydrates in the presence of SO2, CH4, N2, and H2S impurities" The Journal of Chemical Thermodynamics, 2012.

This thesis is structured as follows. The second chapter contains all AFGP research including the following sections; introduction, methodology, computational details, results and discussion, and conclusion. The third chapter contains all Clathrate research including the subsequent sections; introduction, methodology, computational details, results and discussion, and finally the conclusion. The fourth chapter contains a summary of the conclusions and future work related to the studies performed in this work. References are found at the end of every chapter, respectively.

(1) Leach, A. R. *Prentice Hall* **1996**.

(2) Duan, Y.; Kollman, P. A. *Science* **1998**, *282*, 740-744.

(3) Levy, Y.; Onuchic, J. N. In *Annual Review of Biophysics and Biomolecular Structure*; Annual Reviews: Palo Alto, 2006; Vol. 35, p 389-415.

(4) Noskov, S. Y.; Roux, B. *Biophysical Chemistry* **2006**, *124*, 279-291.

(5) Bouvet, V.; Ben, R. N. *Cell Biochemistry and Biophysics* **2003**, *39*, 133-144.

(6) Czechura, P.; Tam, R. Y.; Dimitrijevic, E.; Murphy, A. V.; Ben, R. N. *Journal of the American Chemical Society* **2008**, *130*, 2928-2929.

(7) Tam, R. Y.; Ferreira, S. S.; Czechura, P.; Chaytor, J. L.; Ben, R. N. *Journal of the American Chemical Society* **2008**, *130*, 17494-17501.

(8) Tam, R. Y.; Rowley, C. N.; Petrov, I.; Zhang, T. Y.; Afagh, N. A.; Woo, T. K.; Ben, R. N. *Journal of the American Chemical Society* **2009**, *131*, 15745-15753.

(9) Sloan, E. D. *Journal of Chemical Thermodynamics* **2003**, *35*, 41-53.

(10) Alavi, S.; Woo, T. K. *Journal of Chemical Physics* **2007**, *126*, 7.

(11) Adeyemo, A.; Kumar, R.; Linga, P.; Ripmeester, J.; Englezos, P. *International Journal of Greenhouse Gas Control* **2010**, *4*, 478-485.

(12) Linga, P.; Kumar, R.; Lee, J. D.; Ripmeester, J.; Englezos, P. *International Journal of Greenhouse Gas Control* **2010**, *4*, 630-637.

Chapter 2: Investigating ice recrystallization inhibition activity of novel cryprotectants

Introduction

The development of new cryoprotectant products and cryopreservation protocols are imperative to meet the ever increasing demand for donor organs.[1] Due to the shortage of donor organs, twenty (20) recipient candidates die each day waiting for a transplant in the United States of America alone.[2] Although failure to receive organ transplants is not the leading cause of mortalities, the number of candidates waiting for organs continues to dominate the number of viable donor organs available. This gap has widened dramatically since the 1990s.[2] Cryopreservation is a technique with an essential role in applications such as tissue, blood and long term organ storage and preservation.[3-5]

Presently, the most significant barrier preventing mass organ cryopreservation and storage is that safe and long-term technologies do not exist. However, there are several methodologies and products currently being explored and further developed. Current cryopreservation techniques consist of using additives such as dimethyl sulfoxide.[6-11] Unfortunately, these methods are impractical and unveil safety problems. For example, with the use of DMSO as a cryoprotectant, it becomes evident that the latter is cytotoxic at concentrations above 5%. The cytotoxicity of the following product is strongly temperature dependent and as a result, the temperature regulation during the cryogenic processes (heating and cooling) must be strictly regulated to avoid deterioration of cellular viability.[3,4,6-15]

Another contributing process which compromises cell safety during cryopreservation is the formation of large intra and intercellular ice crystals *in vivo*.[5,16] This process occurs during the cooling, storage, and warming cycles of cryopreservation.[5,16] Currently, organs are stored at hypothermic temperatures during transportation and also during short-term storage before the transplant procedures.[5,16] There are multiple cases demonstrating that the cold temperatures themselves are not causing damage to the cells but rather the formation of large sharp ice crystals inside and/or outside the cell that lead to cellular injury. This process is known as ice recrystallization.[5,16]

The idea behind cryopreservation is to eventually be able to store and preserve blood as well as whole organs indefinitely. Optimizing the latter technique will minimize the number of organs that spoil in inventory.[5,16] It is known that when cooling cells, their metabolic functions decelerates and their degradation is minimized. As previously mentioned, if the cold temperature is not the reason for compromising cell viability, theoretically it should be possible to lower temperatures such that long term storage and preservation can be achieved.[5,16]

One particular factor that controls the formation of these sharp ice crystals inside and outside the cell is believed to be the rate of cooling; this process may dictate cellular viability during cryopreservation. Once temperatures have reached zero degrees Celsius at atmospheric pressure, the spontaneous formation of ice in pure water becomes favourable. The formation process of ice crystals requires a group of water molecules to arrange in such a way that forms a stable crystalline nucleus (solid phase). Water molecules (liquid phase) can then attach to the existing ice crystal nucleus allowing it to grow as long as the conditions remain in favour of spontaneous ice formation for pure water.

Vitrification of pure water can occur once temperatures of -138 degrees Celsius are reached; the latter state consists of an amorphous solid state avoiding the formation of any ice crystalline structures making it ideal for cryopreservation.[17] There are two known ways to reach the vitrification of pure water without the formation of any ice crystals. The first is extremely rapid cooling of pure water to the glass transition state. The second is the use of additives (impurities) that prevent the formation of stabilized ice nuclei therefore inhibiting ice crystal growth.[5,18] Unfortunately, with current technologies, the first method must be disregarded, as flash freezing rates necessary for this application (10^6 °C/sec) are only possible on the micron scale. Consequently, organ cryopreservation is not possible.[5,18]

It is well established that adding impurities to water creates a freezing point depression (colder temperatures are required to freeze pure water) thus allowing water to achieve lower temperatures without increasing the probability of ice formation.[19] Therefore, impurities titled ice recrystallization inhibitors or cryoprotectants can potentially increase cell viability during cryopreservation by minimizing ice crystal formation. The notion of the ice recrystallization inhibition (IRI) potential of a cryoprotectant is a measure of its effectiveness to minimize ice crystal formation and ice crystal size. Experimentally, ice crystal grain size is the parameter used to evaluate the IRI potential of a given compound. For example, cryoprotectants that are IRI active result in the formation of small ice crystals (small mean grain size), while IRI inactive compounds result in the formation of large ice crystals (large mean grain size). This property is of importance because it is believed that the smaller sharp ice crystals cause less damage to cells once formed inside or outside the cell walls. Unfortunately, little is known on the recrystallization mechanism of ice, therefore an

investigation into the fundamental factors responsible for affecting ice recrystallization is vital for the future of cryopreservation. However, the fundamental problem with current cryoprotectants is that the typical concentrations required to prevent ice recrystallization at cryogenic temperatures are deemed cytotoxic.

A certain variation to cryopreservation can be found in one of nature's harshest environments; the arctic tundra. This region is home to a biodiversity of flora and fauna capable of withstanding the harshest temperatures.[20-23] For example, arctic waters can exhibit temperatures below the freezing point of pure water at atmospheric pressure all year yet life manages to thrive. Researchers Scholander and DeVries were the first to investigate this phenomenon in polar fish. The analysis of the latter's blood led to the conclusion that an increased concentration of ions (impurities) accounted for only 40-50 % of the demonstrated freezing point depression.[24-27] After careful analysis, it was established that the reason for the remaining freezing point depression was a result of certain glycoproteins.[28-31] Concentrations near 25 mg/ml of glycoproteins are typically found in a variety of polar fish such as *Trematomas borgrevinki* and *Dissostichus mawsoni*.[32] The latter compounds were classified as AntiFreeze GlycoProteins (AFGPs) which typically consist of a repeating (Ala-Ala-Thr) polypeptide backbone capable of having minor sequence variations.[32] Moreover, a variety of carbohydrates are bound to a hydroxyl oxygen on the amino acid residues located in the backbone.[32] Figure 2.1 depicts the structure of a naturally occurring AFGP.

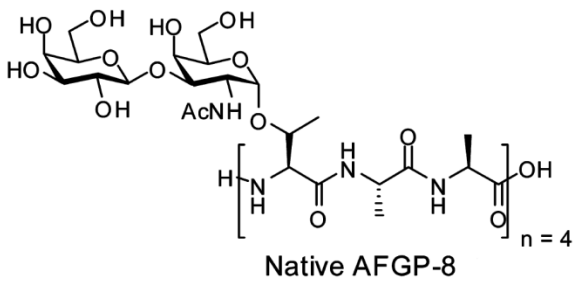

Figure 2.1: Structure of native AFGP-8 from *Gagus Ogac. n* represents the number of repeating units in the backbone. Reproduced from reference [33] [33]

Since AFGPs were discovered, many diverse antifreeze glycoproteins have been identified in numerous arctic species. Currently, there are a wide variety of AFGPs being studied derived from many different fish such as Arctic cod or Antarctic notothenioids.[23,32,34,35]

Unfortunately, the exact reasons and mechanisms of ice recrystallization inhibition and freezing point depression with AFGPs are still unclear. Although there is no concrete mechanism that explains these features, many early studies believed that the proposed mechanism of action for other cryoprotectants may be similar to that of the AFGPs.[32] Previously, it was perceived that the antifreeze glycoproteins would insert themselves by means of hydrogen bonding where the hydroxyl groups located in the carbohydrate moieties would directly interact with the ice lattice. This process would disrupt the addition of any new water molecules to the solid phase, therefore ceasing the ice crystal growth.[32] This mechanism is very similar to the colligative effect demonstrated by solutes in low concentration solutions. However, it was quickly disregarded as it did not account for all of the outstanding freezing point depressions observed in the polar species. More recently, other plausible propositions for this mechanism of action have been an important topic of concern when regarding AFGPs as cryoprotectants.[32] As of late, Ben *et al*. have suggested a new

mechanism of action for ice recrystallization inhibition of AFGPs while utilizing two general concepts. The first concept is that bulk water is present between every formed ice crystal (Nucleation site of ice).[36] The second concept is that the transition between the ice lattice and bulk water interface is not abrupt.[36] The latter concept has recently received much attention; it is proposed that the existence of a semi-ordered layer of ice denoted the quasi-liquid layer (QLL) is located between the highly ordered ice lattice (solid) and the highly disordered bulk water (liquid).[37,38] Notions of the novel layer are growing rapidly and according to infrared studies by Sadtchenko *et al*., the thickness of the layer is determined to be inversely proportional to the temperature.[38] Furthermore, the latter study also observed that in conditions similar to those of polar ocean waters, the QLL is roughly ~1 nm.[38] The result of such a thin QLL suggests that if a solute is present it will have a significant effect on the entirety of the water ordering in the quasi-liquid layer. Recently, many studies have concentrated on the implications of the QLL's fundamental role in the ice recrystallization inhibition (IRI) mechanism. Consequently, it has been suggested that the inhibitors do not directly interact with the ice lattice but instead interact at the quasi-liquid layer level to disrupt the ice crystal growth.[36] The reasoning behind this theory is as follows; The formation of larger ice crystals are believed to be a two step transition process where water molecules from the bulk water (highly disordered zone) must enter the QLL (moderately disordered zone). Molecules from the quasi-liquid layer can then attach to the growing ice lattice (highly ordered zone).[37,38] It is now believed that the IRI mechanism functions by disturbing the ordered structure in the QLL. This makes it very difficult and energy intensive for disordered water molecules in the bulk and QLL phases to enter the more ordered ice lattice (see figure 2.2).[39] In addition, Uchida *et al*. have studied the mechanism of action for IRI activity for certain cryoprotectants. They have suggested that the cryoprotectants in

question carry out their function at the bulk water and QLL interface, therefore consolidating the previous statements and hypotheses.[40]

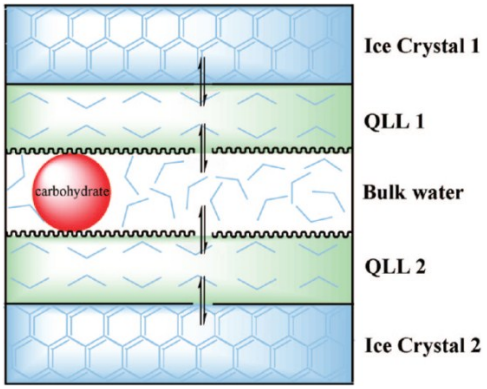

Figure 2.2: Schematic representation of the quasi-liquid layers. Carbohydrate resides at the QLL–bulk water interface between two different ice crystals. Carbohydrate preserves the disordered nature of the surrounding bulk water. This prevents bulk water molecules from entering the more ordered QLL phase, halting the addition of any water molecules to the highly ordered crystal phase. As a result, ice crystal growth is terminated. Reproduced from reference [36][36]

Working towards a better understanding of AFGPs and their mechanism of action, Ben *et al*. have recently tested and characterized many native fish AFGPs as well as AFGP analogues.[33,39] Some of their latest studies compare the efficiency of different native AFGPs. However, due to the difficulty of synthesizing these compounds and their bioavailability, it is desirable that more synthetically accessible analogues be used instead.[41] Ben *et al*. have suggested many different methods for creating AFGP analogues, two of which have received considerable attention as they have shown very promising results. Their studies consist of substituting the carbohydrate moiety with other carbohydrates not present in native AFGPs. Also, their studies consist of varying polypeptide backbone and side chain lengths (see figure 2.3. The analogues are then screened for IRI efficacy.[33,36,39,41]

There is still a lack of understanding as to why certain analogues are more efficient at inhibiting ice recrystallization. Some of the AFGPs synthesized by Ben *et al*. have demonstrated very similar IRI efficacy as nature however, alternatively some derivatives can lead to a complete absence of IRI activity.[33,36,39,41] IRI efficacy of native AFGP-8 and some of its analogues are shown in figure 2.3. It is clear that native AFGP-8 is the most IRI active compound as it results in the formation of the smallest ice crystal mean grain size, followed by analogue 3 and 5.

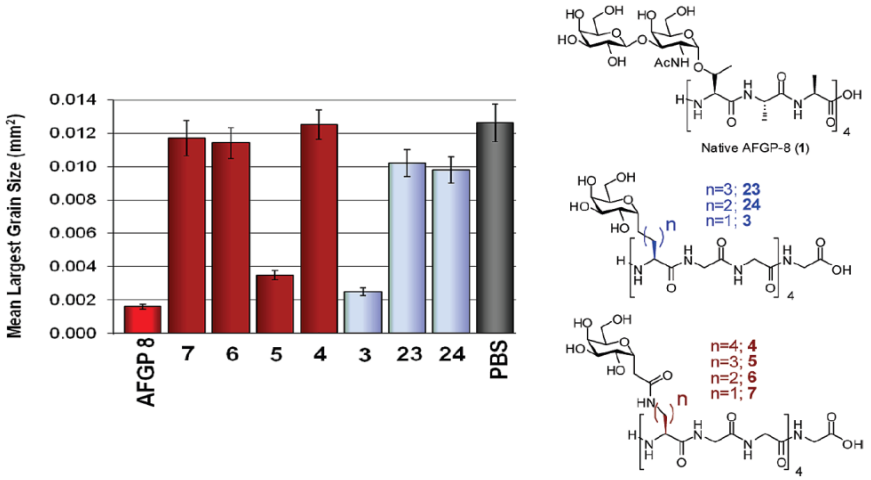

Figure 2.3: Recrystallization inhibition activity in terms of mean grain size of native AFGP-8 and some of its analogues. A phosphate buffered saline solution acts as a control. *n* represents the number of carbons in the side chain for the different analogues. Error bars are shown for all derivatives. Reproduced from reference [39] [39]

Furthermore, due to the cryoprotectant nature of carbohydrates and their ability to dictate ice recrystallization inhibition efficacy in AFGPs, studies solely on the IRI activity of carbohydrates were conducted in hopes of acquiring a more fundamental understanding.[36] Ben *et al.'s* most recent efforts have focused on correlating known and obvious properties to ice recrystallization inhibition activity. In early 2008, the Ben lab observed that by varying the saccharide on the AFGP, different IRI activity could be realized. The difference in

efficacy was believed to be attributed to the hydration number of the solute in question, which is the number of water molecules in the hydration shell (water molecules that are forced to presume order due to solute interactions).[39] Interpreting these results lead to the following hypothesis; The more water a solute displaces (larger partial molar volumes) the more disordered the water surrounding the solute becomes in terms of the proper ordering for insertion into the ice lattice. This prevents the addition of any new water molecules to the ice crystal thus ceasing growth. Results from Ben *et al.'s* study demonstrate moderate correlation between the hydration number and IRI activity. On the contrary, slight offsets are evident when comparing solutes with very different molecular size.[36]

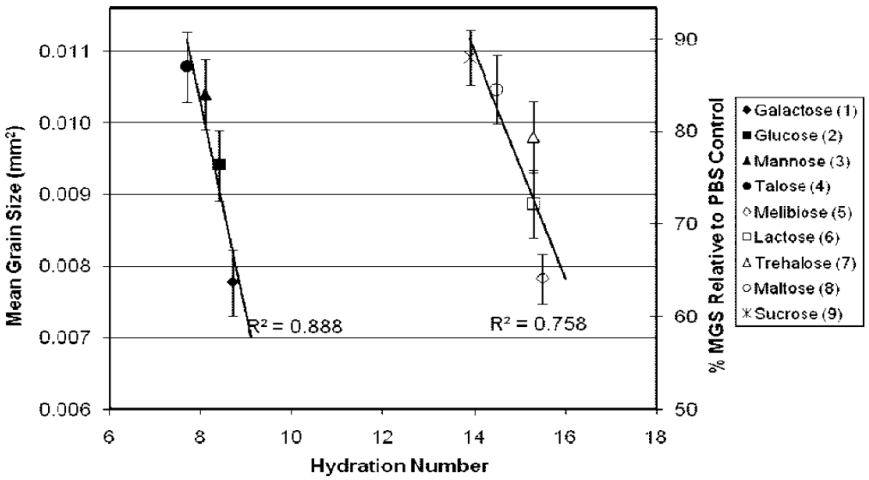

Figure 2.4: Recrystallization inhibition activity in terms of mean grain size of various monosaccharides and disaccharides as a function of their hydration number. Reproduced from reference [36] [36]

In figure 2.4, the IRI potential in terms of mean grain size is plotted against the hydration number for a series of carbohydrates (mono and disaccharides). It is evident that there is a strong linear correlation between the hydration number and the IRI efficiency. Recall, smaller mean grain size translates to smaller ice crystals, thus potent ice

recrystallization inhibitors. On the other hand, the increase in hydration number between the mono and disaccharides did not necessarily translate to greater IRI efficacy.

Further into 2008, Ben *et al*. discovered the reason behind the offset in their hydration number correlation theory between mono and disaccharides. By incorporating the volume of the solute and the hydration number, the offset between largely different molecular sizes would disappear and one prevalent trend would emerge. This new property was termed the hydration index.[36] Ben *et al.* utilized this parameter using the hydration number divided by the partial molar volume (volume for 1 mole of solute given a specific solvent) of the solute in question. Thus, the hydration index is interpreted as being the number of tightly bound water molecules per molar volume of solute (see figure 2.5). As a result of the latter correction, mono and dissacharides can be unified under a single parameter (the hydration index) as a means of evaluating the ice recrystallization inhibition potential.

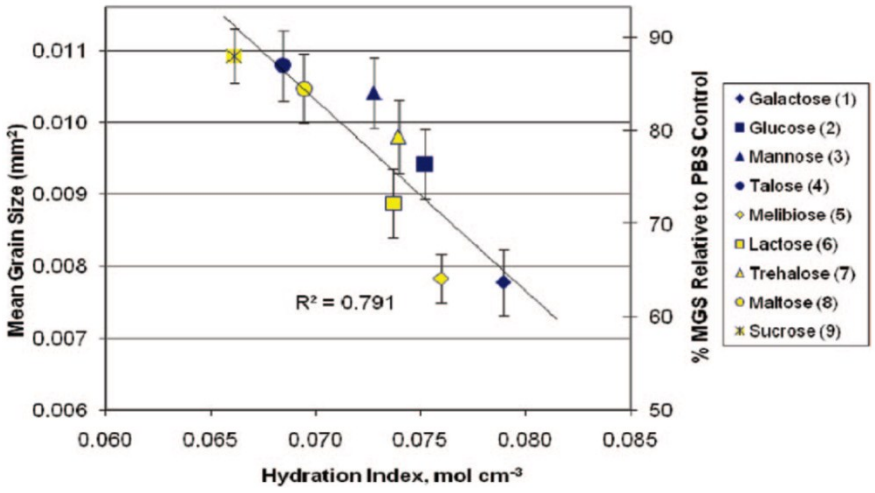

Figure 2.5: Recrystallization inhibition activity of various monosaccharides and disaccharides as a function of their hydration index. Trend between mono and dissacharides is unified as they are normalized in terms of partial molar volume. Reproduced from reference [36] [36]

If the IRI ability can be related to the hydration index, then it was thought that molecular dynamics simulations of the saccharides in water could be used as a means to probe the hydration index of a species. For example, one could examine the hydrogen bonding between the solute and water to estimate the hydration number. As previously mentioned, AFGPs have limited bioavailability and AFGP analogues are difficult to synthesize; thus, it would be desirable to use computational resources to screen potentially efficient AFGPs, and to provide potentially useful insight for novel cryprotectant design. Previous simulation efforts by Ben *et al*. are limited to solution conformations of AFGPs and their analogues using classical molecular dynamics simulations. In 2009, the Woo and Ben groups published an experimental and computational study of a variety of AFGP analogues. Solution conformations of numerous analogues derived from native AFGP-8 were calculated using MD simulations with the AMBER-9 simulation package.[39] The analogues were solvated by TIP3P water in the NTP ensemble and the intramolecular hydrogen bonding between the galactose moiety and the backbone were studied.[39] In brief, they observed the intramolecular hydrogen bonding differences between potent IRI analogues and non-potent IRI analogues. They concluded that persistent hydrogen bonding between two hydroxyl groups located in the carbohydrate moiety was solely present in non-active AFGP analogues, whereas the IRI active counterparts demonstrated very little hydrogen bonding (see figure 2.6). This may indicate that the hydroxyl-water interactions may be crucial to IRI activity, in such a way that strong hydrogen bonding between the hydroxyl groups results in weak hydroxyl-water interactions. Therefore leaving the surrounding water undisturbed causing weak IRI activity.[39]

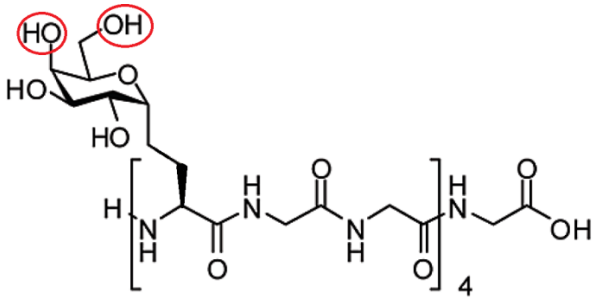

Figure 2.6: Structure of AFGP-8 analogue; Circled are the two hydroxyl groups in the carbohydrate moiety participating in hydrogen bonding.

Moreover, the distance between the carbohydrate moiety and the polypeptide backbone was also investigated and revealed that potent inhibitors exhibit shorter distances than weak inhibitors.[39] Findings by Rowley *et al.* demonstrated that the distance between the carbohydrate moiety and the polypeptide backbone (shown in figure 2.7) presented a direct correlation to cryogenic performance for a small set of AFGP analogues, although the test set was too small to make any definitive conclusions (shown in figure 2.7).[33] When I started my thesis work, I tested the correlations between the IRI activity and the properties obtained from MD simulations on a larger test set of AFGP analogues more recently synthesized by the Ben lab. Although the experimentally determined hydration indices were still found to correlate well with the IRI activity, the correlations determined from the MD simulations broke down on this larger data set of AFGP analogues. Thus, we set out to determine if we could calculate the hydration index developed by Ben's lab directly from MD simulations.

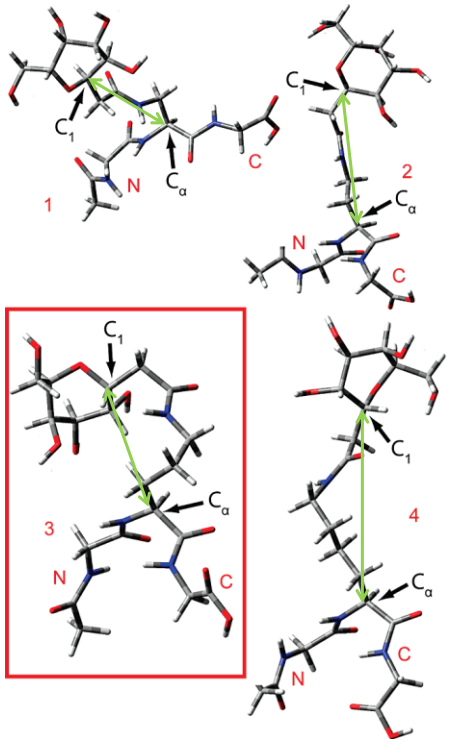

Figure 2.7: Snapshots of the MD conformations for 4 different analogues. Analogue 3 has the shortest carbohydrate-backbone distance. It is also the most potent ice recrystallization inhibitor. Reproduced from reference [39] [39]

Objectives:

Since Ben and coworkers found that the IRI efficacy could be correlated with the so-called hydration index of a AFGP analogue, the goal of my initial thesis project was to determine if we could accurately calculate the hydration index from molecular dynamics simulations. This would involve determining the partial molar volume and the hydration number from such simulations. Rather than attempt to evaluate the hydration index on AFGP analogues, our initial goal was to determine if the hydration indices could be determined from MD simulations for the carbohydrate components of selected AFGP analogues developed in the Ben lab; specifically talose, mannose, galactose, and sucrose (figure 2.8). The carbohydrates alone also exhibit IRI activity that Ben and coworkers were also able to

correlate to the hydration index. Thus, simulations on the carbohydrate component rather than the whole AFGP analogue would simply test the calculations, but still allow for a meaningful examination of the efficacy of the methodology. If hydration indices for the sugars could be calculated accurately, then calculations of the whole AFGP analogue would then be performed. If the hydration index of AFGPs could be evaluated from simulation, then these calculations could be a valuable tool for predicting and screening new AFGP analogues before significant effort is put towards their synthesis.

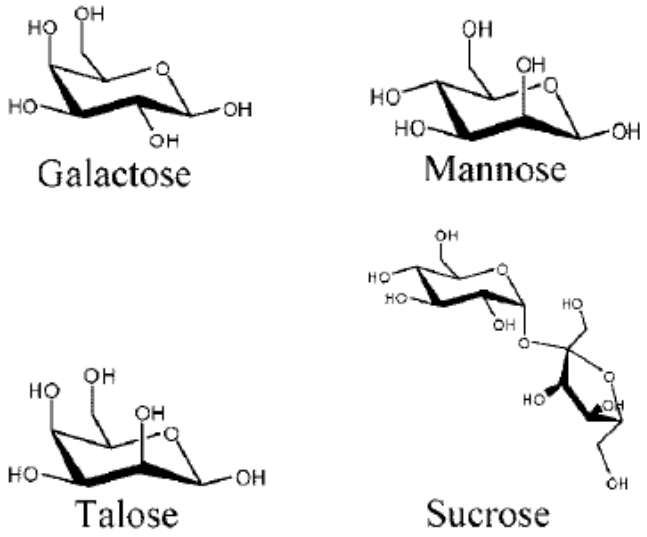

Figure 2.8: Test structures of carbohydrates studied in this work.

In the next section of this chapter, the background theory and methodology for calculating the hydration index will be presented. This will be followed by the computational details of the simulations performed. The results and discussion section of our efforts will follow with the chapter ending in a conclusion section.

Methodology

Recall, the initial goal of this work is to directly evaluate the hydration index for a set of carbohydrates (i.e. talose, mannose, galactose and sucrose). Ben and coworkers developed this index to correlate well to IRI activity of AFGP analogues.[39] The group defines the hydration index as:[36]

$$hydration\ index = \frac{n_h}{V_\varphi} \qquad 2.1$$

where n_h is the hydration number of the solute (in our case the carbohydrate) in water and V_φ is the partial molar volume of the solute at infinite dilution.[36] First, let us dissect the hydration index into two separate calculations, V_φ being the partial molar volume and n_h being the hydration number.

The initial step in this procedure is to evaluate the partial molar volume (PMV) V_φ at infinite dilution which is equivalent to the apparent partial molar volume (volume observed in solution depending on its mole composition).[42] This property is defined by:[43]

$$V_\varphi = 1000\,{(d_0 - d)}\Big/{(M \cdot d \cdot d_0)} + {MM}/{d} \qquad 2.2$$

where d_0 and d are the densities of the pure water and the carbohydrate solution, respectively; M is the molality of the carbohydrate in solution; and MM is the molar mass of the carbohydrate.[43] It is evident from equation 2.2 that three (3) variables are required to directly evaluate the partial molar volume: d_0, d and M. First, the molality M in equation 2.2 can be easily calculated knowing the composition of the system with the following relation:[42]

$$M = \frac{n_{solute}}{m_{solvent}} \qquad 2.3$$

where n_{solute} is the number of moles of solute (i.e. carbohydrate) in the solution and $m_{solvent}$ is the mass of the solvent (i.e. water) in the solution. Secondly, to calculate the partial molar volume in equation 2.2, one would need to evaluate the density, d of the carbohydrate solution. This can be accomplished by means of classical molecular dynamics simulations of the solute in water.[44] The average density value of the solution in question is then extracted over the entirety of the simulation.[44-46] This results in the direct evaluation of d (carbohydrate solution density) and d_0 (pure water density). Calculating the partial molar volume by means of classical MD completes the first step in the procedure for determining the hydration index.

The second step in evaluating the hydration index requires the hydration number n_h of equation 2.1 defined as:[43]

$$n_h = \left({}^{x_0}/_{x}\right)\left(1 - {}^{\beta_s}/_{\beta_{s0}}\right) \qquad 2.4$$

where x_0 and x in this case are the mole fractions of water and solute (carbohydrate), respectively for the solution in question. β_{s0} and β_s of equation 2.4 are the isentropic partial molar compressibility coefficients of pure water and the carbohydrate solution, respectively.[43] The isentropic partial molar compressibility coefficient β_s is the measure of how compressible a solution is depending on its composition at constant entropy.[42] Equation 2.4 requires the evaluation of four variables to directly calculate the hydration number x_0, x, β_s and β_{s0}. The mole fractions are easily calculated knowing the composition of the system with the following relation:[42]

$$x_i = \frac{n_i}{n_{tot}} \qquad 2.5$$

where i represents pure water (x_0) or the carbohydrate (x), therefore n_i is the number of moles of the constituent of interest (pure water or carbohydrate) and n_{tot} is the total number of moles in the system (i.e. moles of water in the case of pure water and moles of pure water added to the moles of carbohydrate in the case of solutions).[42]

The biggest challenge in calculating the hydration index from simulation involves determining the final variable in equation 2.4, the isentropic partial molar compressibility coefficients, β_s. This property is defined as:[43]

$$\beta_s = \left(-\frac{1}{V}\right)\left(\frac{dV}{dP}\right)_s \qquad 2.6$$

where the variation of the volume V with respect to pressure P is under constant entropy s.[43]

Unfortunately, molecular dynamics simulations at constant entropy are not standard simulations making these calculations problematic. Fortunately, at ambient temperatures and lower, the isentropic partial molar compressibility, β_s, is nearly equal to the isothermal partial molar compressibility, β_T:[47]

$$\beta_s = \left(-\frac{1}{V}\right)\left(\frac{dV}{dP}\right)_s \approx \beta_T = \left(-\frac{1}{V}\right)\left(\frac{dV}{dp}\right)_T \qquad 2.7$$

Figure 2.9 shows the variation of β_T and β_s for water as a function of temperature.[47] The isothermal partial molar compressibility is potentially more accessible to simulation as conventional NPT ensembles (constant number of particles, pressure and temperature) could be utilized.

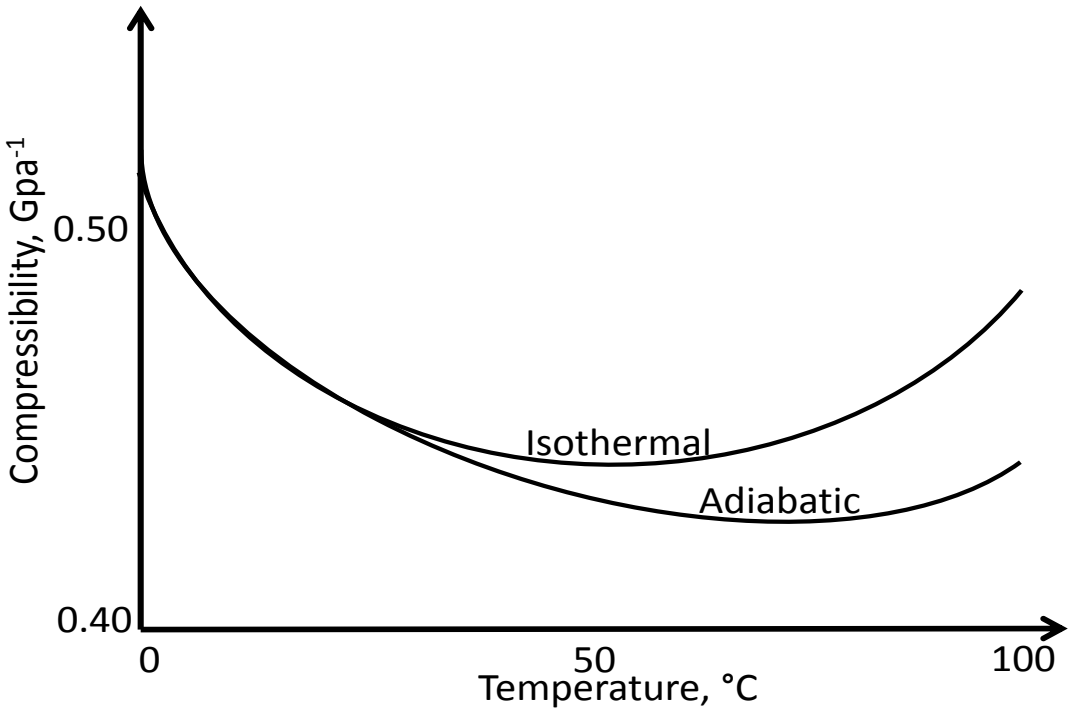

Figure 2.9: Isothermal and adiabatic compressibilities of water. Isothermal and adiabatic compressibilities of water are nearly equivalent at 25 °C.[47]

There are several literature examples that study the partial molar volume and use the isentropic partial molar compressibility coefficients to estimate the hydration number of carbohydrates in water. For example, Galema and coworkers experimentally estimated the partial molar volumes and hydration numbers for a series of carbohydrates in 1991.[43] The latter study utilized the isentropic methodology presented in equation 2.2 and 2.4, and according to their results, they provided exceptionally accurate partial molar volumes and hydration numbers.[43] Due to the accuracy of this study and the relation presented in equation 2.7, the isothermal partial molar compressibility should be a plausible approximation to the isentropic molar compressibility at room temperature yielding similar accuracy.

Using classical molecular dynamics simulations in the NTP ensemble, the isothermal partial molar compressibility coefficients can be determined more readily by the fluctuation relationship with the following equation:[48]

$$\beta_T = \left(-\frac{1}{V}\right)\left(\frac{dV}{dp}\right)_T \approx \beta_T = \langle\frac{\sigma_V^2}{K_B T V}\rangle_{NTP} \qquad 2.8$$

Where σ_V is the average variance of the volume for a given simulation; K_B is the Maxwell-Boltzmann constant; T is the temperature; and V is the average volume of the simulation.[48]Once the value of β_T is evaluated using classical molecular dynamics simulations, it can be substituted in equation 2.4 along with the mole fractions to evaluate the hydration number.

Recall, to directly evaluate the hydration index (equation 2.1) the partial molar volume (equation 2.2) and the hydration number (equation 2.4) are required. The methodology detailed above demonstrates the procedure to directly evaluate the hydration index.

More recently, Voth and coworkers have evaluated the isothermal partial molar compressibility coefficients of different water models and found that most models accurately predict this value.[49] Voth and coworkers attempted to evaluate the isothermal partial molar compressibility more directly by evaluating the variation of the volume with respect to pressure using the finite difference approximation given by:[49]

$$\beta_T = \left(-\frac{1}{V}\right)\left(\frac{dV}{dp}\right)_T \approx \beta_T = \left(\frac{\ln^{d_2}/_{d_1}}{P_2 - P_1}\right)_T \qquad 2.9$$

where d_2 is the density corresponding to pressure P_2 and d_1 is the density corresponding to pressure P_1.[49] Unlike the fluctuation method, this method requires multiple simulations to

evaluate the isothermal partial molar compressibility coefficients. Finite difference procedures begin by utilizing a typical NPT simulation at ambient conditions to extract the equilibrium density d_{eq} of the system.[49] In addition, two NVT ensemble simulations (constant number of particles, volume and temperature) are required.[49] One equates to density d_2 defined as: [49]

$$d_2 = d_{eq} + 0.04 \text{ g/cm}^3 \qquad 2.10$$

the other simulation equates to density d_1 defined as: [49]

$$d_1 = d_{eq} - 0.04 \text{ g/cm}^3 \qquad 2.11$$

These simulations provide the necessary data to evaluate β_T using equation 2.9. Pressures P_2 and P_1 can be extracted from the simulations of d_2 and d_1, respectively. This method provides an alternative route for evaluating the hydration index with the isothermal partial molar compressibility.

Both the fluctuation approach and the finite difference approach will be investigated in this work as to standardize the procedure for these types of studies.

Computational details

Description of model systems

The main objective in this work is to determine the hydration index of various carbohydrates (i.e. Glactose, mannose, talose, sucrose) using classical molecular dynamics simulations. This section will provide the specifications necessary to reproduce the simulations used in this work.

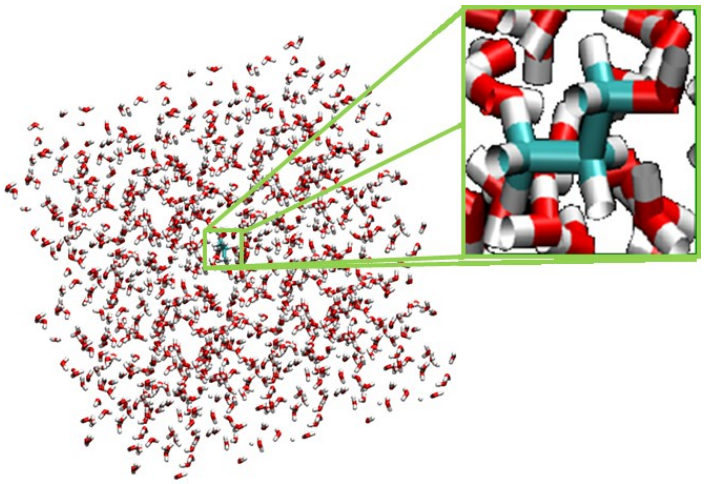

Figure 2.10: Snapshot of a simulation cell of a solvated carbohydrate surrounded by TIP3P water. Boxed area represents a close up of the solvated carbohydrate in the simulation cell.

The simulations in this project were performed using the AMBER-9 simulation package and consist of a single carbohydrate (i.e. Glactose, mannose, talose, sucrose) solvated by water as depicted in figure 2.10. The initial step in creating these systems requires the insertion of the carbohydrate at the center of the orthorombic simulation box with cell dimensions of 32.0*x*33.0*x*34.0 Å. All carbohydrate configurations were built using Glycam's Carbohydrate 3D Structure Predictor on the glycam website.[50] This supplied the necessary pdb files containing carbohydrate structures for our simulations.[50] The next step in

constructing our simulations requires the solvation of the carbohydrates with TIP3P water using the built-in AMBER Solvate Box program. The latter program incrementally adds water molecules into the simulation box provided while crosschecking a designated radius around the newly inserted water molecule ensuring that there is no overlap with any other molecules in the simulation cell.[45] A 16 Å parameter describing the distance between the carbohydrate and the edge of the simulation box was used with the solvate box program, adding roughly 3300-3350 water molecules. Periodic boundary conditions were utilized to approximate the bulk solution.

A complication for these simulations is the necessity of infinite dilution. Due to the nature of this study, the properties of interest (i.e. PMV) depend solely on the contributions of one carbohydrate interacting with its hydration shell. To truly satisfy infinite dilution (defined as no solute-solute interactions) the carbohydrates must not directly (carbohydrate-carbohydrate interaction) or indirectly (hydration shell-hydration shell interaction) interact with one another.[51] As previously mentioned, periodic boundary conditions replicate the system creating multiple carbohydrates in the simulation. Altough, non-bonded cut-offs can be used to eliminate the Van der Waals interactions between solute molecules, there will still be long ranged electrostatic interactions between periodic images.

The electrostatics in the simulation were governed by the Point-Charge model derived by using a standard AM1-BCC method reproducing RESP charges[52,53] calculated at a Hartree-Fock/6-31G* level of accuracy. The Glycam force field developed by Woods and co-workers is used to describe inter and intra molecular interactions within and between

carbohydrates.[54] Glycam is a specialized force field developed for carbohydrates.[54] A typical TIP3P rigid potential was used to define water interactions in the system.[55]

Simulations were also performed using the DL_POLY 2.17 simulation package. For reasons described later on in this work, DL_POLY was used to simulate the alcohols propanol, propanediol, hexanol, and hexanediol in water. Simulations consisted of a single alcohol solvated by water in a cubic simulation cell of length 45.0 Å. Alcohol structures optimized at the empirical level using the Generalized Amber Force Field were used for all simulations. Once again, the alcohols were then solvated with TIP3P water, this time using the built-in DL_POLY Water Add program. Unlike AMBER's Solvate Box program, DL_POLY's Water Add requires only simulation cell vectors, inserting roughly 1950-3350 water molecules in our simulation cell. The program does so by replicating the simulation cell with the same dimensions and fills it with water molecules. The next step in the Water Add Program combines the simulation cell containing the alcohol and the simulation cell containing the water and systematically removes any water molecules that overlap with the solute.[46] Unlike the Amber model, DL_POLY simulations utilized a different force field to define inter and intra molecular interactions. Instead of the Glycam force field, the Generalized AMBER Force Field was used to describe inter and intra molecular interactions within and between alcohols.[56] GAFF is a more generalized force field that can treat a wider range of general organic compounds.[56] Furthermore, the performance and efficiency of the GAFF parameters have been successfully tested to properly represent the conformations, energies and dynamical properties for multiple organic species including alcohols.[56] Finally, periodic boundary conditions, point charges, Van der Waals interactions, the water model used in the AMBER simulations were used with DL_POLY.

The Amber & DL_POLY simulation packages used in this study utilize the Leap Frog-Verlet algorithm to integrate the equations of motion.[45] The initial configurations generated from Amber and DL_POLY solvation codes were first optimized. For the Amber calculations on the carbohydrates, the AMBER-9 simulation package was used. For these simulations, the systems were first equilibrated under constant temperature and pressure conditions for 100 ps. The simulation times for the production runs were a nanosecond or greater. These simulations were performed under ambient conditions with temperatures and pressures set to 293 K and 1 atm, respectively. All bonds involving hydrogen atoms were frozen using the SHAKE algorithm, to allow for the use of a large timestep of 1.0 fs. Ewald summations were used in all simulations to quickly treat long ranged Coulombic interactions. The Nosé/Hoover thermostat/barostat was utilized in this work with a thermostat constant of 5.0 ps^{-1}, and a barostat constant of 0.5 ps. Finally, a 12 Å non-bonded cutoff was employed to reduce the number of non-bonded interactions.

In addition to NPT simulations, NVT simulations were used in this study to investigate two (2) different calculation methodologies for determining the partial molar compressibility coefficients. The fluctuation method presented by Galema and co-workers was evaluated in the NPT ensemble and the finite difference method presented by Voth was evaluated in the NVT ensemble. For the NVT simulations, the simulation parameters were identical to those previously mentioned except that the volume was fixed in the simulations.

As previously mentioned, the finite difference method requires multiple simulations, one simulation in the NPT ensemble providing the equilibrium density, and two (2) simulations in the NVT ensemble at different densities. These two different simulations were performed at slightly different densities (d_2 defined as $d_2 = d_{eq} + 0.04$ g/cm^3 and d_1

defined as $d_1 = d_{eq} - 0.04$ g/cm^3) where d_{eq} is the density of the system at equilibrium determined from the NPT simulation. The resulting configuration from the NPT simulations served as an initial configuration for the NVT simulations. Similar to NPT simulation, an equilibration run in the NVT ensemble served to make the transition between the NPT ensemble and the NVT ensemble smoother.

Results and discussion

The most reliable parameter used to correlate ice recrystallization inhibition activity is the hydration index developed by Ben et al. This property is based on the hydration number and the partial molar volume. The objective in this work was to directly evaluate the hydration index by means of calculating the partial molar volume and hydration number. This was done by using the fluctuation and finite difference methods via classical molecular dynamics simulations. The following section presents and discusses our findings.

The first simulations attempted in this work utilized the AMBER-9 simulation package in the NPT ensemble, at 293 K and 1 atm, to simulate the solvation of various carbohydrates defined by the Glycam force field. These simulations were performed to evaluate the partial molar volume for a series of carbohydrates. Our results are presented in table 2.1 and compared to experimental data found in the literature.

Table 2.1: Theoretical partial molar volumes vs partial molar volumes from this work (numbers in parentheses represent errors on the partial molar volume)[43]

	Galema and Hoiland	***Our work***
Systems	**Partial Molar Volume (cm^3mol^{-1})**	**Partial Molar Volume (cm^3mol^{-1})**
Talose	112.5 (0.1)	108.5 (169)
Mannose	111.3 (0.2)	108.5 (168)
Galactose	110.2 (0.3)	96.4 (170)
Sucrose	211.6 (0.3)	195.9 (171)

From table 2.1, we see there is reasonable agreement between the simulated data and the literature values presented in the work of Galema and Hoiland. However, due to the large error margins of the method (numbers in parentheses in table 2.1) the data also shows that the simulated results are not likely capable of distinguishing between any carbohydrates.

These results led to further investigation and revealed a fundamental problem with the density extracted from our simulations. It was observed that the density values for different carbohydrates are only slightly different (on the order of 10^{-4}). Consequently, density errors on a similar order (10^{-4}) produce indistinguishable differences between the carbohydrates. Due to the strong dependence of the partial molar volume to the density (see equation 2.2), the PMV values become erroneous.

To address this problem, an understanding of the density inaccuracy is required. The density is directly proportional to volume and pressure, thus any unexpected fluctuations can strongly affect this value. In fact, this is precisely the case in our NTP simulations. Pressure fluctuations are occurring on such a large scale that errors on the density are relatively large (10^{-3}). Errors such as these render our simulations untenable for evaluating the partial molar volume. Therefore, more precise and accurate means to regulate the pressure in the system is necessary. Regulating the barostat relaxation constant proved futile in the attempt to obtain more converged densities. As a result of our previous efforts, it was thought that the problem lay in the Langevin thermostat/barostat used in AMBER. This thermostat/barostat does not rigorously sample the NPT ensemble due to the nature of the scaling.[45] The technique randomly selects one molecule and scales its kinetic energy to regulate the changes in temperature and pressure.[45] This results in the occurrence of potentially unphysical equilibrium behaviour and it was thought that this may be causing problems in the convergence of the densities.[45]

Another common thermostat/barostat method used in classical molecular dynamics simulations is the Nosé/Hoover method.[46] This method scales the kinetic energy of all the molecules as to formally sample the NPT ensemble.[46] Unfortunately, this thermostat/barostat

is not implemented in the AMBER-9 simulation package. For this reason, the DL_POLY simulation package, which utilizes the Nosé/hoover barostat/thermostat, was used for further calculations. Moreover, it was thought that the imprecision in the density is due to the pressure regulation in AMBER. Another contributing factor to the erratic pressure can also be a result of the ill-defined force field used to describe intra and inter molecular interactions. Although the Glycam force is optimized for treating carbohydrates, these molecules are notoriously difficult to simulate, in part due to their conformational variability. To more easily determine the sources of error in calculating the partial molar volume, we decided to simulate simple alcohols which are expected to have more refined and accurate force fields. The previous changes in the force field, simulation package, and thermostat/barostat should eliminate all variables that can result in unreliable pressure. Therefore, accurate densities and thus partial molar volumes can be extracted from future simulations.

The remainder of the simulations performed in this study utilized the DL_POLY 2.17 simulation package along with the Generalized Amber Force Field and Nosé/Hoover thermostat/barostat to simulate the solvation of various alcohols (i.e. propanol, propanediol, hexanol and hexanediol) at 293 K and 1 atm. Partial molar volume results are presented in table 2.2 and compared to experimental data found in the literature.

Table 2.2: Theoretical partial molar volumes vs partial molar volumes from this work (numbers in parentheses are errors on the partial molar volume)[51]

	Hoiland	***Our work***
Systems	**Partial molar volume (lit.) (cm^{-3} mol^{-1})**	**Partial molar volume (calc.) (cm^{-3} mol^{-1})**
Propan-1-ol	70.65 (0.05)	56.61 (202)
Propanediol-1,3	71.93 (0.05)	51.73 (152)
Hexan-1-ol	117.96 (0.05)	72.24 (159)
Hexanediol-1,3	120.01 (0.05)	95.05 (158)

Unfortunately, results presented in Table 2.2 show clear discrepancies between the simulated data in this work and the literature values presented in the work of Hoiland.[51] Similar to the carbohydrate results in Table 2.1, the error margins on the partial molar volume of the alcohols prevent us from distinguishing between molecules. Further investigation revealed the same density related problem as the AMBER calculations on carbohydrates. In the case of the alcohols, the density errors are also on the orders of 10^{-3} whereas the density differences between different alcohols are only on the order of 10^{-4}. This is illustrated in figure 2.11.

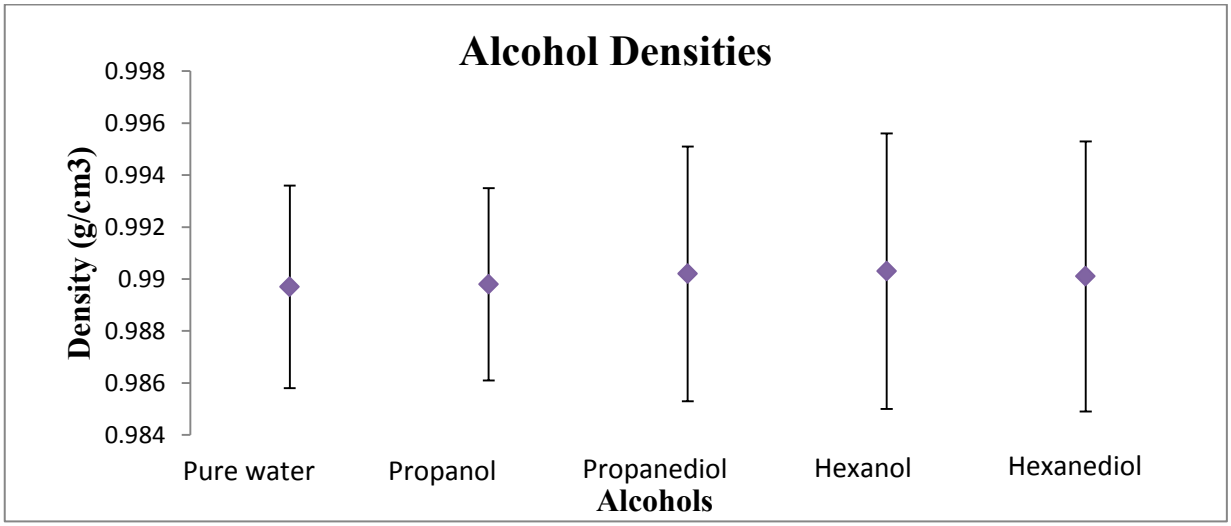

Figure 2.11: Density error analysis for all alcohols extracted from DL_POLY simulations using GAFF and the Nosé/Hoover thermostat/barostat. Density error bars are shown for all alcohols. It is clear that all densities are within error making them indistinguishable between one another.

The reoccurring difficulties with the density inspired a literature investigation on both experimental and computational studies attempting to determined partial molar volumes of molecules. Among multiple studies, we discovered that all evaluations of the partial molar volumes are conducted at concentrations much larger (3 to 6 times) than the concentration

used in this work (infinite dilution 0.0177 molal).[59-62] Typical molal concentrations found in the literature vary anywhere between 0.05 and 0.1 molal resulting in accurate PMV results experimentally.[59-62] However, these concentrations are no longer considered infinite dilution, therefore solute-solute interactions must be accounted for while evaluating the partial molar volume. Usually this is accomplished by measuring the density for a series of different concentrations and extrapolating to infinite dilution. Figure 2.12 and table 2.3 summarize our efforts in dealing with larger concentrations in hopes of achieving better PMV accuracies.

Simulations were no longer performed at infinite dilution; instead specific molal concentrations used to determine the partial molar volume experimentally were replicated in hopes of obtaining greater accuracies.

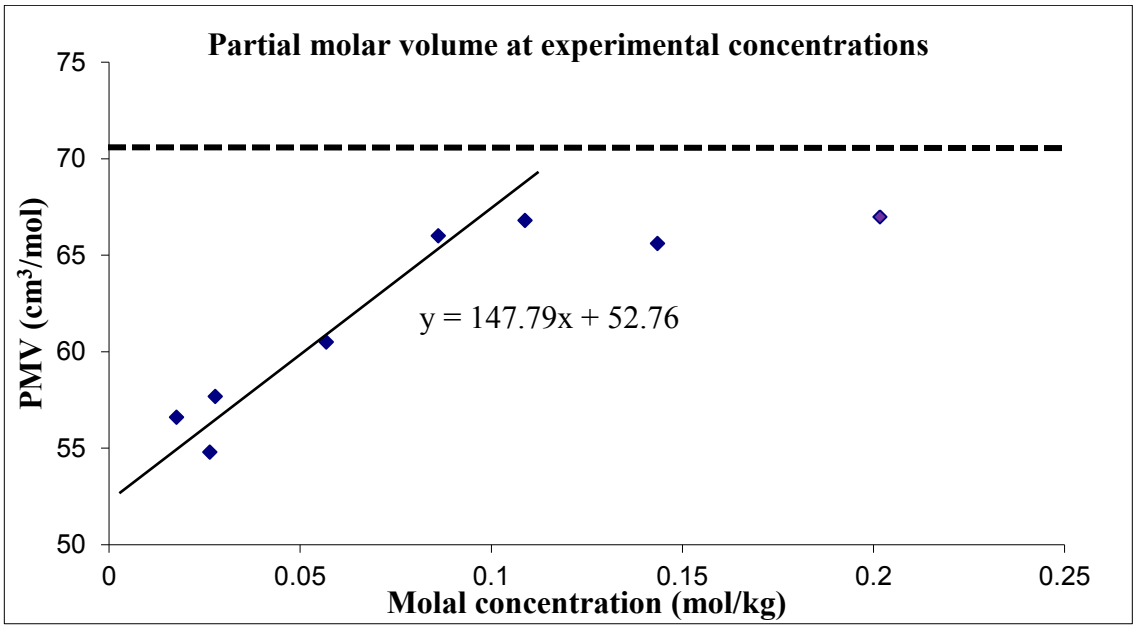

Figure 2.12: Partial molar volume of propanol at different concentrations. Dotted line represents the experimental literature value of the partial molar volume of propanol at infinite dilution. Solid line represents the extrapolation to infinite dilution from our simulations.

Table 2.3: Partial molar volume of propanol at different simulated concentrations.

Number of alcohols molecules	Number of water molecules	Molality (mol/kg)	Partial molar volume (cm^3/mol)
1	3143	0.0177	56.6
1	2116	0.0264	54.8
2	3921	0.0278	57.7
2	1934	0.0569	60.5
3	1934	0.0862	66.0
4	1934	0.1089	66.8
5	1934	0.1435	65.6
7	1934	0.2017	67.0

Figure 2.12 illustrates the partial molar volume extracted from the simulations submitted at different concentrations. It is clear from the results that the limiting concentration for classical molecular dynamics simulations is reached at a concentration of roughly 0.0862 molal. The partial molar volume of propanol converges to a value of ~ 66.0 cm^3/mol. The dotted line in figure 2.12 represents the experimental literature value of the PMV for propanol at infinite dilution (70.65 cm^3/mol). Unfortunately, the literature value and our calculated value are not very comparable (20% error). Errors such as these are not acceptable especially for evaluating the PMV, where very accurate and precise values are required in order to distinguish between solutes that are very similar in structure (i.e. propanol vs propanediol). More importantly, the partial molar volume difference between stereochemically different carbohydrates such as galactose and mannose will not be accessible.

Due to the increased concentration required to achieve the detection limit, PMV results extracted from MD simulations are further discredited. Although this increase in concentration generated more accurate partial molar volumes of 66.0 cm^3/mol as opposed to 56.61 cm^3/mol, simulations performed at the limiting concentration no longer satisfy the

condition of infinite dilution. Figure 2.13 represents propanol at concentrations in the detection limit of molecular dynamics simulations. It is clear from this figure that solute-solute interactions are present in the system, thus the partial molar volume extracted from these simulations are not representative of the PMV at infinite dilution. To obtain a more representative value for the partial molar volume at infinite dilution, the data evaluated for the different concentrations must be extrapolated. The extrapolation (solid line) is shown in figure 2.12, leading to a calculated PMV of 52.76 cm^3/mol.

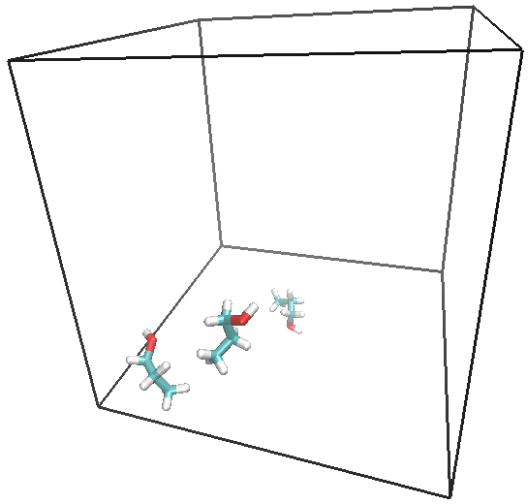

Figure 2.13: Simulation cell illustrating solute-solute (propanol) interactions at the limiting concentration of molecular dynamics simulations; water molecules have been omitted for clarity. It is evident that the alcohols are grouping together.

In addition to our study, a thorough literature review revealed many sources studying solvated alcohols, alcanes, and carbohydrates with molecular dynamics simulations.[59-62] These studies also determined volumetric properties such as partial molar volume and revealed similar problems in reproducing experimental partial molar volumes. In-depth investigations of these studies reveal similar density issues as our research.[59-62] This confirms that the accuracy obtained in this work is the limit of molecular dynamics simulations. [59-62]

Unfortunately, simulated densities are not comparable to experimental results. Consequently, the volumetric properties of interest such as the PMV will be inaccurate. These inaccuracies will translate directly to inaccuracies in the hydration index making any correlations to the ice recrystallization inhibition activity impossible. These results show that MD simulations cannot be used to calculate the hydration indices using the methods outlined.

Conclusion

Previously, Ben et al observed that ice recrystallization inhibition efficacy is correlated to the hydration index. This parameter is based on the partial molar volume and hydration number for a prospective cryoprotectant. Classical molecular dynamics simulations were used to investigate these volumetric properties for carbohydrates such as galactose, mannose, talose, sucrose, and alcohols including propanol propanediol, hexanol and hexanediol. These simulations were performed in hopes of facilitating and standardizing the screening protocol of possible novel antifreeze compounds. After 8 months of rigorous testing, a clear conclusion can be drawn.

The use of classical molecular dynamics simulations to investigate volumetric properties such as the partial molar volume and hydration number is not possible due to the heavy dependence on density. The density of a solution is highly dependent on the concentration of the solute in question as is the partial molar volume. This work illustrates that the accuracy and precision of the density extracted from simulations is not sufficient to distinguish between similar compounds.

The partial molar volume of a compound relies fundamentally on one variable property; density. These densities can be extracted by simulating the solutions of interest. However, classical molecular dynamics simulations demonstrate a detection limit which is the threshold for distinguishing similar properties of different species. Unfortunately, the detection limit for the density in classical molecular dynamics simulations is much greater than the density differences of different species at infinite dilution, thus accurate partial molar volumes cannot be extracted.

To conclude, this work demonstrates clearly that current classical molecular dynamics technology cannot probe the volumetric properties of interest with sufficient accuracy to aid in the research and development of novel cryoprotectants.

(1) Hafez, T. F., B.; Baust J. G.; Baust J. M. *CRC press: Boca Raton* **2007**, 197-210.

(2) Transplantation, U. S. G. I. o. O. a. T. D. a. *http://organdonor.gov/* **2011**.

(3) Mazur, P. *American Journal of Physiology* **1984**, *247*, C125-C142.

(4) Mazur, P.; Leibo, S. P.; Chu, E. H. Y. *Experimental Cell Research* **1972**, *71*, 345-&.

(5) Fowler, A.; Toner, M. In *Cell Injury: Mechanisms, Responses, and Repair*; New York Acad Sciences: New York, 2005; Vol. 1066, p 119-135.

(6) Eroglu, A.; Bailey, S. E.; Toner, M.; Toth, T. L. *Biology of Reproduction* **2009**, *80*, 70-78.

(7) Hossain, A. M.; Osuamkpe, C. O. *Archives of Andrology* **2007**, *53*, 99-103.

(8) Hunter, J. E.; Bernard, A.; Fuller, B.; Amso, N.; Shaw, R. W. *Human Reproduction (Oxford)* **1991**, *6*, 1460-1465.

(9) Mondal, B. *Cell and Tissue Banking* **2009**, *10*, 341-344.

(10) Wezeman, F. H.; Guzzino, K. M. *Cryobiology* **1986**, *23*, 81-87.

(11) Whittingham, D. G. *Journal of Reproduction and Fertility* **1977**, *49*, 89-94.

(12) Davis, J. M.; Rowley, S. D.; Braine, H. G.; Piantadosi, S.; Santos, G. W. *Blood* **1990**, *75*, 781-786.

(13) Elmoazzen, H. Y.; Poovadan, A.; Law, G. K.; Elliott, J. A. W.; McGann, L. E.; Jomha, N. M. *Cell and Tissue Banking* **2007**, *8*, 125-133.

(14) Liseth, K. A., J. F.; Bjorsvik, S.; Grottebo, K.; Bruserud, O. *Cryotherapy* **2005**, *7*, 328-333.

(15) Ohlendorf, C.; Tomford, W. W.; Mankin, H. J. *Journal of Orthopaedic Research* **1996**, *14*, 413-416.

(16) Gage, A. A. B., J. *Cryobiology* **1998**, *61*, 3149-3158.

(17) Turnbull, D. *Solid State Physics-Advances in Research and Applications* **1956**, *3*, 225-306.

(18) J.M., B. *Cell preservation technology* **2002**, *1*, 17-31.

(19) Turnbull, D. *Journal of Physical Chemistry* **1962**, *66*, 609-&.

(20) DeVries, A. L. *Biochemical and Biophysical perspectives in marine biology* **1974**, 289-330.

(21) Duman, J. G.; Olsen, T. M. *Cryobiology* **1993**, *30*, 322-328.

(22) Graham, L. A.; Liou, Y. C.; Walker, V. K.; Davies, P. L. *Nature* **1997**, *388*, 727-728.

(23) Yeh, Y.; Feeney, R. E. *Chemical Reviews* **1996**, *96*, 601-617.

(24) Devries, A. L.; Wohlschl.De *Science* **1969**, *163*, 1073-&.

(25) Devries, A. L. K., S.K.; Feeney, R.E. *Journal of biological chemistry* **1970**, *245*, 2901-2908.

(26) Gordon, M. S.; Scholander, P. F.; Amdur, B. H. *Biological Bulletin* **1962**, *122*, 52-&.

(27) Scholander, P. F.; Vandam, L.; Kanwisher, J. W.; Hammel, H. T.; Gordon, M. S. *Journal of Cellular and Comparative Physiology* **1957**, *49*, 5-24.

(28) Duman, J. G.; Devries, A. L. *Cryobiology* **1972**, *9*, 469-472.

(29) Lin, Y.; Devries, A. L.; Duman, J. G. *Biochemical and Biophysical Research Communications* **1972**, *46*, 87-&.

(30) Raymond, J. A.; Devries, A. L. *Cryobiology* **1972**, *9*, 541-547.

(31) Scholand.Pf; Maggert, J. E. *Cryobiology* **1971**, *8*, 371-&.

(32) Harding, M. M.; Anderberg, P. I.; Haymet, A. D. J. *European Journal of Biochemistry* **2003**, *270*, 1381-1392.

(33) Tam, R. Y.; Rowley, C. N.; Petrov, I.; Zhang, T. Y.; Afagh, N. A.; Woo, T. K.; Ben, R. N. *Journal of the American Chemical Society* **2009**, *131*, 15745-15753.

(34) Feeney, R. E.; Burcham, T. S.; Yeh, Y. *Annual Review of Biophysics and Biophysical Chemistry* **1986**, *15*, 59-78.

(35) Fletcher, G. L.; Hew, C. L.; Davies, P. L. *Annual Review of Physiology* **2001**, *63*, 359-390.

(36) Tam, R. Y.; Ferreira, S. S.; Czechura, P.; Chaytor, J. L.; Ben, R. N. *Journal of the American Chemical Society* **2008**, *130*, 17494-17501.

(37) Karim, O. A.; Haymet, A. D. J. *Chemical Physics Letters* **1987**, *138*, 531-534.

(38) Sadtchenko, V.; Ewing, G. E. *Journal of Chemical Physics* **2002**, *116*, 4686-4697.

(39) Czechura, P.; Tam, R. Y.; Dimitrijevic, E.; Murphy, A. V.; Ben, R. N. *Journal of the American Chemical Society* **2008**, *130*, 2928-2929.

(40) Uchida, T.; Nagayama, M.; Shibayama, T.; Gohara, K. *Journal of Crystal Growth* **2007**, *299*, 125-135.

(41) Liu, S. H.; Ben, R. N. *Organic Letters* **2005**, *7*, 2385-2388.

(42) Petrucci, R. H. H., F.G.; Madura, J.D.; Bissonnette, C. *Pearson* **2011**, *10*, 214,560.

(43) Galema, S. A.; Hoiland, H. *Journal of Physical Chemistry* **1991**, *95*, 5321-5326.

(44) Leach, A. R. *Prentice Hall* **1996**.

(45) Amber9 *Reference manual*.

(46) DL_POLY2.17 *Reference manual*.

(47) Zemansky, M. W. D., R.W. *McGraw-Hill Book Company* **1981**, *6*, 238.

(48) McQuarrie, D. A. *Harper and Row* **1976**.

(49) Wu, Y. J.; Tepper, H. L.; Voth, G. A. *Journal of Chemical Physics* **2006**, *124*, 12.

(50) http://glycam.ccrc.uga.edu/ccrc/carbohydrates/cb_newbuilder.jsp.

(51) Hoiland, H. *Journal of Solution Chemistry* **1980**, *9*, 857-866.

(52) Cieplak, P.; Cornell, W. D.; Bayly, C.; Kollman, P. A. *Journal of Computational Chemistry* **1995**, *16*, 1357-1377.

(53) Cornell, W. D.; Cieplak, P.; Bayly, C. I.; Kollman, P. A. *Journal of the American Chemical Society* **1993**, *115*, 9620-9631.

(54) Woods, R. J.; Dwek, R. A.; Edge, C. J.; Fraserreid, B. *Journal of Physical Chemistry* **1995**, *99*, 3832-3846.

(55) Jorgensen, W. L.; Chandrasekhar, J.; Madura, J. D.; Impey, R. W.; Klein, M. L. *Journal of Chemical Physics* **1983**, *79*, 926-935.

(56) Wang, J. M.; Wolf, R. M.; Caldwell, J. W.; Kollman, P. A.; Case, D. A. *Journal of Computational Chemistry* **2004**, *25*, 1157-1174.

(57) Case, D. A.; Cheatham, T. E.; Darden, T.; Gohlke, H.; Luo, R.; Merz, K. M.; Onufriev, A.; Simmerling, C.; Wang, B.; Woods, R. J. *Journal of Computational Chemistry* **2005**, *26*, 1668-1688.

(58) Case, D. A. e. a. *University of California* **2006**, *San Francisco*.

(59) Avdeev, M. V.; Bodnarchuk, I. A.; Petrenko, V. I.; Kholmurodov, K. T.; Yaradaikin, S. P. *Russian Journal of Physical Chemistry A* **2009**, *83*, 1129-1133.

(60) Romero, C. M.; Paez, M. S.; Arteaga, J. C.; Romero, M. A.; Negrete, F. *Journal of Chemical Thermodynamics* **2007**, *39*, 1101-1109.

(61) Romero, C. M.; Paez, M. S.; Perez, D. *Journal of Chemical Thermodynamics* **2008**, *40*, 1645-1653.

(62) Sangwai, A. V.; Ashbaugh, H. S. *Industrial & Engineering Chemistry Research* **2008**, *47*, 5169-5174.

(63) Baruch, E.; Belostotskii, A. M.; Mastai, Y. *Journal of Molecular Structure* **2008**, *874*, 170-177.

(64) Furuki, T. *Carbohydrate Research* **2000**, *323*, 185-191.

(65) Furuki, T. *Carbohydrate Research* **2002**, *337*, 441-450.

(66) Galema, S. A.; Howard, E.; Engberts, J.; Grigera, J. R. *Carbohydrate Research* **1994**, *265*, 215-225.

Chapter 3: Investigating the feasibility of sI clathrate hydrates as carbon capture tools

Introduction

Carbon capture and storage (CCS) represents a serious strategy to reduce the environmental impact of energy production by capturing CO_2 from the combustion gas and permanently storing it. The development of new carbon capture materials and carbon capture protocols are imperative to the struggle of mitigating the ever increasing temperature of earth's atmosphere. For over two hundred years, mankind has been releasing increasing amounts of greenhouse gases (GHG) such as methane, carbon oxides, nitrous oxides and chloro/fluorocarbons into the atmosphere[1]. These gases are capable of retaining infrared (IR) radiation inside earth's atmosphere causing temperatures to climb.[1] The increased release of GHG in the last century alone has resulted in a 0.74 °C rise in average global temperature.[2] Among many concerns associated with the rise in temperature, global sea levels and vegetation viability are the most important. The aforementioned increase in temperature has resulted in a 17 cm increase in average global sea levels due to thawing polar ice caps and glaciers.[2] Consequently, global warming has become one of the leading environmental and political concerns today. Many political efforts have attempted to regulate the latter by implementing strategies such as the Kyoto protocol established in 1997 by the United Nations Framework Convention on Climate Change (UNFCCC).[3,4] The latter requires those whom have ratified to reduce their GHG emissions by 5.2 % of their 1990 emission level.[3,4] For these reasons, carbon capture and storage techniques/materials play an essential role in the future of earth's climate.

World energy demands and the cost (real and perceived) associated with the start-up of new technologies for energy production mean that fossil fuels will continue to be used for power generation. Therefore, high levels of CO_2 will continue to be emitted from flue stacks in combustion plants despite the many concerns raised about global warming. Coal combustion for power generation alone produces 7 gigatonnes of anthropogenic CO_2 per year.[5] This is equivalent to 40% of all anthropogenic CO_2 emission yearly.[5] Fortunately, CO_2 is one of the weaker GHGs as it can only absorb a small spectrum of infrared radiation. Although CO_2 is not considered a particularly potent greenhouse gas (GHG), its importance is due to its escalating concentration in the atmosphere making it the largest contributor of anthropogenic GHG to global warming. For this reason, CCS has attracted serious attention. Numerous pilot programs exist in the struggle for carbon capture and storage. For example, some commercial coal plants have been retrofitted with CO_2 carbon capture technology. Nonetheless, large scale CCS is not yet realized.

At the moment, the most significant barrier to large scale CCS from coal burning power plants is that low energy and cost effective CO_2 scrubbing technologies do not exist. However, several methodologies are being explored and developed. One CO_2 scrubbing method widely used today is based on aqueous amines, such as mono or diethanolamine. These solutions are used to capture the CO_2 from the flue gas by means of chemisorption.[6] Once CO_2 and the aqueous amine interact, a chemical reaction can occur. This process is based on the following reactions where R is the remaining atoms in a typical amine:[7]

$$CO_2 + NRH_2 \rightarrow N^+RH_2COO^- \qquad 3.1$$

$$N^+RH_2COO^- + NRH_2 \rightarrow RH_2NCOO^-\,NRH_2^+ \qquad 3.2$$

Although presently the most commonly used CCS method, in order to recover the liquid amine sorbent, heating of the solution is required. This process is energetically costly. Furthermore, the liquid amine solution is toxic, corrosive, and degrades over time due to irreversible side reactions with other flue gases. Consequently, the aqueous amine solvent must be replaced at a rate of eight pounds per ton of CO_2 captured, adding to the overall cost of clean energy production.[6] Today, incorporating aqueous amine scrubber technology in power plants usually translates to a drop in power generating efficiency (roughly 30 %) per combustible fuel. This is due to the parasitic energy load of the carbon capture mechanism making alternatives to this approach desirable.[8]

Another technology that has received great attention is the use of nanoporous solids to capture CO_2 (g) in flue gas post-combustion. Such solids include zeolites (Zeolitic Imidazolate Framework) and metal organic frameworks (MOFs). Unlike liquid amines, nanoporous solids interact with the flue gas by means of adsorption.[9,10] These materials are porous crystalline solids with well-defined cavities. They can be tuned to tailor pore size, accessibility, gas selectivity, and gas uptake simply by substituting the fundamental building blocks in the framework such as metal linkers and organic ligands. Flue gas derived from the coal burning process is allowed to diffuse through a compartment containing the nanoporous material. In which case, the gases (i.e. CO_2) have the opportunity to adsorb to certain sites in the framework by means of non-bonded (dispersion and/or electrostatics) interactions. The CO_2 saturated material can then be regenerated by multiple means such as pressure swing or temperature swing techniques. The most common method utilizes a combination of the two techniques. In these processes, adsorption usually occurs at a given temperature and pressure.

However, desorption of CO_2 is forced at greater temperatures and lower pressures than those used for adsorption. The newly freed carbon dioxide gas can now be compressed, stored or transported in a separate container. The desorption process regenerates the nanoporous solid for recycled use in future capture. A schematic representation of a zeolite containing adsorbed CO_2 is exemplified in figure 3.1.

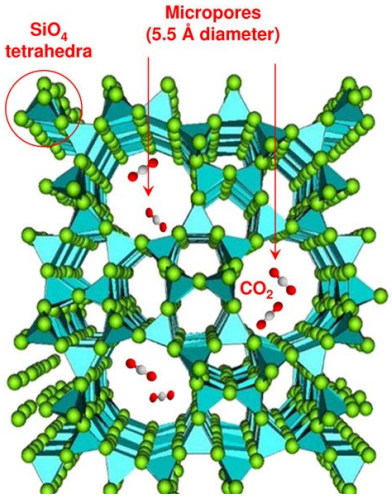

Figure 3.1: SiO_2, silicate structure (zeolite). Carbon dioxide fills the micro-pores of the zeolite under pressure. Reproduced from reference [11] [11]

A problem with the MOF materials (other than their high cost of production) is that they are susceptible to being poisoned by water which is a major combustion product.[12] Moreover, even if the MOF is water stable, it must be significantly more selective for CO_2 than water to effectively capture, separate or store carbon dioxide.[12] One solution for dealing with water is to use a hydrophobic MOF. However, the MOF must also be selective for CO_2 over other non-polar combustion gases such as N_2.[12]

Current technologies for capture and storage have much room for improvement. The challenge now resides in researching and developing novel CCS materials and protocols that can efficiently and effectively remove and store carbon dioxide from the flue gas in coal combustion plants. The development of these technologies are of great importance and crucial in the fight against global warming.

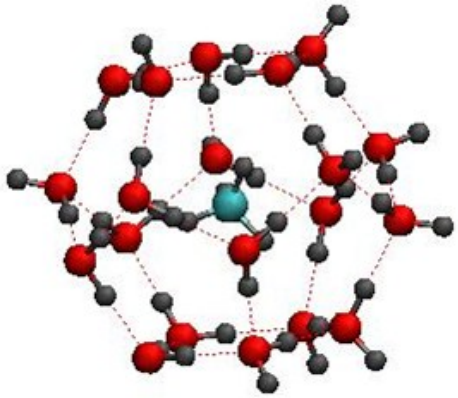

Figure 3.2: Single clathrate hydrate cage encapsulating a methane molecule. Hydrogen bonds between water molecules are represented by dotted lines.

Recently, it has been proposed to use the clathrate hydrate formation potential of CO_2(g) gas under pressure (10-30 bar at 273 K) as a means of CO_2 (g) capture from combustion flue streams.[13,14] At sufficiently high pressures (10 bar) and low temperatures (below 300 K), water begins to form structured crystalline cages around non-polar molecules (i.e. CO_2) called clathrate hydrates (see figure 3.2).[15] Considering ambient conditions, the latter combination of molecules would result in an arrangement such that the non-polar-polar interactions are minimized consequently creating two separate phases with an interacting interface.[16] However, at high pressures and low temperatures the water molecules form ordered cages around the non-polar molecules. These cages form in such a way that maximizes the hydrogen bonds between water molecules and as a result minimizes the

number of interactions with the guest (non-polar) molecule. Figure 3.2 shows the hydrogen bonding network of the clathrate hydrates.

There are two advantages of using clathrate hydrates instead of other novel technologies for CO_2 (g) capture. The first being that the only material needed to capture the gas is water and no other hazardous or expensive materials are involved. The second advantage is that this method is not poisoned by water but rather uses water to capture the gas. Thus, the abundant H_2O found in flue gas will not pose any problems to the operation. Figure 3.3 depicts a plausible clathrate hydrate process for carbon capture. This model can theoretically be retrofitted to existing flue stacks in coal combustion plants. Unfortunately, one problem with using clathrates as carbon capture tools is that pressurizing the flue gas to pressures that promote the spontaneous clathrate formation is energetically costly. At the moment, it is still unclear whether or not this process can be optimized to reduce operation costs. Nonetheless, clathrate hydrate based CO_2 scrubbing processes have been proposed and studied.

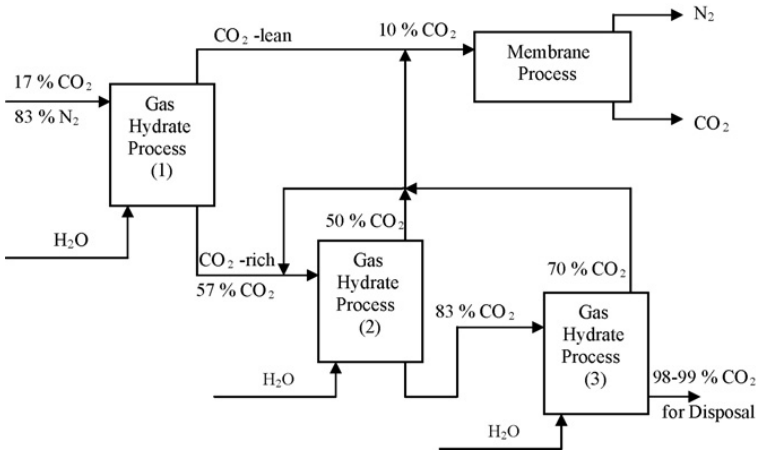

Figure 3.3: Proposed clathrate hydrate apparatus for CO_2 recovery from flue gas exhausted from coal combustion plants. Operational temperature for this apparatus is 273 K. Operational pressure for gas hydrate process 1, 2, and 3 are 10, 5, and 2.5 bar, respectively. Reproduced from reference [17] [17]

Understanding how impurities (gases other than CO_2) present in the flue gas may influence the formation of CO_2 clathrate hydrates is important for using these materials for both carbon capture and storage. These impurities may disrupt CO_2 clathrate formation and/or may impede CO_2 selectivity. For example, Beeskow and coworkers recently studied the effects of 1% SO_2 and NO_2 impurities on the CO_2 hydrate formation process.[18] They found an enrichment of SO_2 in the hydrate phase compared to the gas concentration, which suggests that clathrate hydrate formation also removes these unwanted contaminants from the flue. It was suggested to further investigate the influence of these impurities because they may present some useful features such as promoting hydrate formation at milder conditions (i.e. lower pressure and higher temperature). This can lead to more stable CO_2 clathrate hydrates which can greatly influence the cost for implementing these technologies for CO_2 capture and sequestration. Figure 3.4 represents the pressure and temperature data of CO_2 clathrate formation. It is clear that the conditions required for CO_2 clathrate hydrate formation are reduced in the presence of 1 % SO_2.

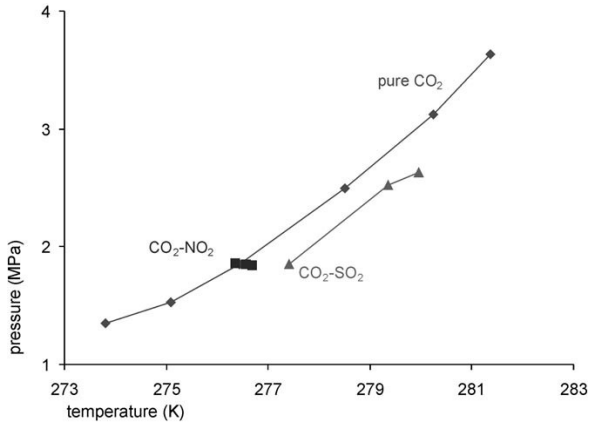

Figure 3.4: Pressure and temperature conditions for hydrate formation. This figure illustrates the clathrate formation diagram for pure CO_2 and CO_2-SO_2 gas mixture. It is clear from this data that the CO_2-SO_2 mixture shifts the clathrate formation temperature to milder values. Reproduced from reference [18] [18]

In the arena of permanent storage, clathrate hydrates may also play a role depending on how the CO_2 is stored. Although the leading strategy for permanent carbon dioxide storage is in depleted oil and gas reservoirs, deep ocean CO_2 storage has also been seriously considered.[19,20] As seen in figure 3.5, once the CO_2 is injected into the deep ocean sediment, it begins to rise due to its buoyancy until it reaches the hydrate formation zone (conditions required for hydrate formation). It then is presumed to form a cap, bottling the remaining buoyant CO_2. Figure 3.6 indicates the potential locations where deep sea storage is possible.

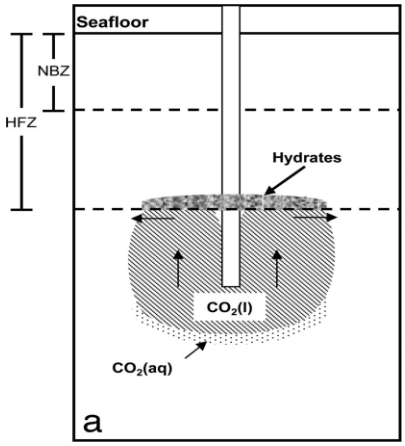

Figure 3.5: Example of carbon dioxide deep sea storage using clathrate hydrate formation potentials to avoid leakage. Hydrates formed in the hydrate formation zone cap rising CO_2, preventing the remaining carbon dioxide from rising. Reproduced from reference [21] [21]

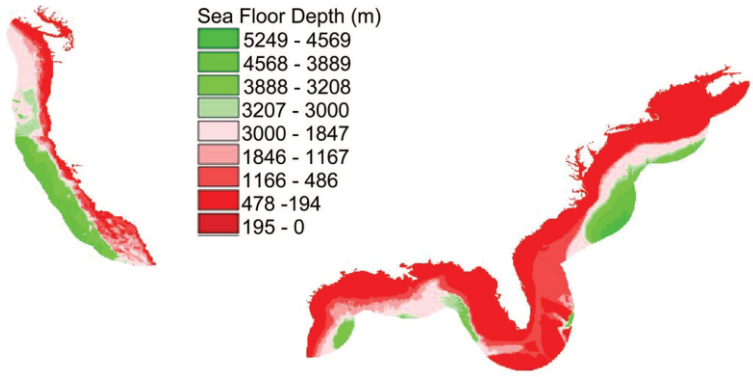

Figure 3.6: Over 22 % of the ocean floor near the United States coast line alone offers favorable conditions necessary for clathrate formation. Reproduced from reference [21] [21]

Furthermore, injection of CO_2 into sediment layers in colder northern climates such as under lakes and ocean beds has been suggested as a route for carbon storage (see figure 3.7) because conditions may be appropriate for hydrate formation.[22-25] Within these processes, the impurities in the flue gas captured and injected with the CO_2 or the existing gases in the injection site, such as methane, may interfere with the CO_2 storage process. It is therefore imperative to explore the phenomena of the clathrate substitution process to gain further insight on the efficacy of certain CCS strategies.

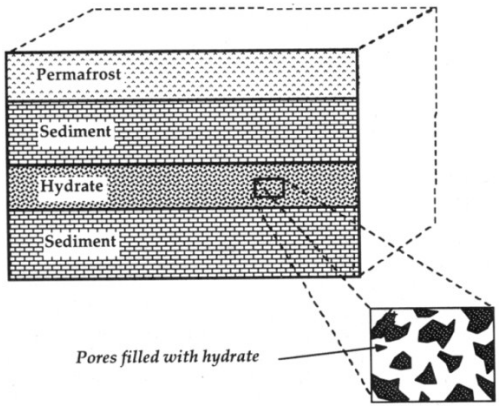

Figure 3.7: Clathrate hydrate reservoir in earth's crust found under northern climate permafrost with favorable hydrate formation conditions. Reproduced from reference [26] [26]

Depending on the temperature, pressure and the non-polar molecule encapsulated, different topologies of clathrate hydrates can form. Under the conditions being proposed for CO_2 capture (273 K and 10 bar), the most stable form of CO_2 clathrate hydrate is the so-called structure I (sI) clathrate hydrate.[13,14] This structure`s unit cell consists of two "small" (S) twelve-sided cages with pentagonal faces [5^{12}] and six "large" (L) fourteen-sided cages composed of twelve pentagonal and two hexagonal sides [$5^{12}6^2$] giving the sI unit cell a formula of $S_2L_6.46H_2O$.[27] The structure of the small and large (S and L in the formula above) sI clathrate hydrate cages are shown in figure 3.8. Each cage can theoretically hold one CO_2

molecule. This translates to a large volumetric efficiency of 1 m^3 per sI clathrate hydrate theoretically capable of storing 172 m^3 of gas.[28] Although, sI clathrate is the stable phase of the hydrate in the suggested CCS application, other phases such as the structure II (sII) and the structure H (sH) do exist. These different phases have different topologies and form at temperatures and pressures between 270-290 K and 15-300 bar depending on the non-polar gas encapsulated.

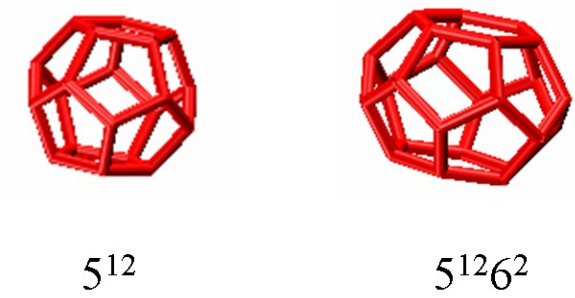

Figure 3.8: The structure of the small (5^{12}) and large ($5^{12}6^2$) cages of the sI clathrate hydrate. The effective diameter of the small cage is 4.84 Å and the major and minor axes of the large cage are 6.12 and 5.07 Å, respectively. Reproduced from reference [27]

Clathrate stabilities and gas substitution thermodynamics have been previously studied via molecular dynamics simulations using Gibbs free energy calculations in hopes of acquiring a more fundamental understanding. More recent efforts entail the study of the Gibbs free energy associated with different guest loadings for various gasses (Ne, Ar, Xe and CH_4). The latter simulations were used to calculate and determine the optimal capacity for storage in these clathrates under different pressure conditions.[29,30] Methane proved to show high uptake in sI clathrate hydrates. More recently, the Woo lab [27,31] have used classical MD Gibbs free energy calculations to examine CO_2 clathrate hydrates under conditions relevant to permanent deep sea storage of CO_2.[21] In the former study, structure H clathrate hydrate stabilities were investigated. The optimal loading was determined at deep sea storage

conditions using classical molecular dynamics studies and thermodynamic integration techniques. The five guest molecules arranged in such a way that minimized the guest-water interactions. Methane substitution reactions for this hydrate were also investigated. The latter methane hydrate proved to be less stable than its CO_2 counterpart demonstrating the potential candidature of structure H clathrate hydrates in the application of CO_2 sequestration. After careful investigation, the study revealed that all CH_4 molecules in the large cages of the clathrate are favourably substituted with CO_2, although the small cages remained un-substituted.

In this work, molecular dynamics simulations will be used to probe the influence of flue gas impurities on the stability of carbon dioxide sI clathrate hydrates. The objective of this work will be to examine the substitution thermodynamics of CO_2 clathrate hydrates with common combustion gases under conditions relevant for CO_2 capture, and related gas purification applications. Flue gas has a weight composition of 65.96% CO_2(g), 8.29 % N_2(g) and Ar(g), 1.28% O_2(g), 0.80 % SO_2(g) and other gases forming fractions of the output.[32] To evaluate the potential of these other gases to disrupt the CO_2 (g) clathrate hydrate formation, we perform a series of molecular dynamics Gibbs free energy calculations based on thermodynamic integration. Our objective will be to determine the relative thermodynamic stability of the different clathrates under the conditions of flue gas. The Gibbs free energies of substituting CO_2(g) with other guests or combinations of other guests will give us insight into the efficiency and practicality of clathrate hydrates as carbon dioxide capture tools in flue stacks. Furthermore, this work studies the substitution of CO_2 for both large and small clathrate hydrate cages to determine which ones are favored sites for substitution with

different guests. The partial (large cage only/small cage only) substitution reactions of the clathrate hydrates will give some indication of the potential for using a binary gas mixture to help promote hydrate formation at milder conditions. This is done in hopes of reducing the cost of implementation as a novel technology for CO_2 gas capture/purification. This study will focus on examining the Gibbs free energies of substituting $CO_2(g)$ with $SO_2(g)$, $H_2S(g)$, $N_2(g)$ and $CH_4(g)$ gasses found in industrial flue streams. These free energies of substitution will be analyzed by dissecting them into Van der Waals, electrostatics, and non-ideal gas components. This will allow us to get further insight on the major factors which contribute to clathrate stability and selectivity. This study was performed in the hopes of understanding the fundamental factors that influence CO_2 clathrate hydrate formation in the presence of impurities under the conditions proposed for post-combustion CO_2 capture.

Methodology

The goal of this work is to examine the substitution thermodynamics of CO_2 clathrate hydrates with an impurity gas Y (i.e. CH_4, SO_2, H_2S, N_2). The difference in Gibbs free energy between the initial state (i.e. CO_2 filled clathrate) and the final state (i.e. Y filled clathrate) is directly correlated to the stability of the system.[16] At constant temperature and pressure, the sign and magnitude of the Gibbs free energy can easily demonstrate the favourability of a change from the initial to the final state.[16] For example, a negative Gibbs free energy difference represents a spontaneous (favourable) process, where the final state of the system is more thermodynamically stable relative to the initial state.[16] A positive Gibbs free energy difference represents a nonspontaneous (unfavorable) process, where the initial state of the system is more thermodynamically stable relative to the final state.[16] Using classical molecular dynamics simulations to extract Gibbs free energy proves to be a practical method for probing the latter substitution thermodynamics. Thermodynamic integration based on classical molecular dynamics is a very useful tool for extracting relative free energy differences between any two given states.[16]

In this work, the thermodynamic integration method used to evaluate the Gibbs free energy is the Kirkwood coupling parameter method.[33] This method utilizes the state function property of the free energy which entails that the free energy difference between two states does not depend on the pathway used to convert the initial state into the final state.[16] Simulations can take full advantage of this property as it allows the construction of artificial states. This may not reflect the actual mechanism (chemical or physical) in which the states are connected. For example, the simulations performed in this study take full advantage of

these artificial states by computationally transforming CO_2 guests into Y guests (i.e. SO_2) inside the sI clathrate hydrate. This is accomplished by slowly modifying the molecules interaction potential. In classical molecular dynamics simulations particles are allowed to evolve through time. The forces that dictate the behavior of a given system are governed by intramolecular interactions U_{bonded} (bonds, angles etc…) and intermolecular interactions $U_{non-bonded}$ (electrostatics and van der Waals). The sum of the intra and intermolecular interactions on every particle in the system results in the potential energy function $U(r^N)$ where r^N represents the position of all particles in the system.(equation 3.3):[34]

$$U(r^N) = U_{bonded} + U_{non-bonded} \qquad 3.3$$

In the simulations performed in this work, we make the approximation that all molecules are rigid. This implies that parameters such as bond lengths, angles etc… are set to fixed equilibrium values. As a result, the parameters are no longer variable throughout the simulation. Recall, that the potential energy function (equation 3.3) depends on both intra and intermolecular interactions. However, the rigid approximation reduces the components of the potential energy function in equation 3.3 solely to intermolecular interactions $U_{non-bonded}$ (equation 3.4).

$$U(r^N) = U_{non-bonded} = U_{elec} + U_{VdW} \qquad 3.4$$

These non-bonded interactions are modeled using electrostatic interactions (charge-charge, charge-dipole, etc…) shown in equation 3.5 and Van der Waals interactions (sterics and dispersions) shown in equation 3.6.

$$U_{elec} = \sum_{i,j} \frac{q_i q_j}{4\pi\varepsilon_0 r_{ij}} \qquad 3.5$$

Where the indices i and j represent all atoms in the simulation; the q terms represent the point charge on the atoms; ε_0 is the permittivity of free space; and r is the internuclear distance between the atoms of interest.[34]

$$U_{VdW} = \sum_{i,j} 4\varepsilon_{ij}\left[\left(\frac{\sigma_{ij}}{r_{ij}}\right)^{12} - \left(\frac{\sigma_{ij}}{r_{ij}}\right)^{6}\right] \quad 3.6$$

Where the indices i and j represent all the atoms involved in the pairwise interactions; ε represents the well depth of the potential energy describing the Van der Waals interactions at equilibrium; σ represents the finite distance between the pairwise interactions where the Van der Waals interaction energy is zero; and r is the internuclear distance between the atoms of interest.[34]

Recall, the goal is to transform one molecule into another using the Kirkwood coupling parameter method by modifying the molecules interaction potential. Furthermore, by utilizing the rigid approximation, we can computationally transform one molecule into another simply by modifying the non-bonded potential $U_{non-bonded}$ according to equation 3.4. Computationally, the general form of the Kirkwood coupling parameter method for a chemical (substitution) or physical (melting) process can be described by the following potential energy function:[34]

$$U(\lambda) = (1-\lambda)U_i(r^N) + \lambda U_f(r^N) \qquad 3.7$$

Where λ is the Kirkwood coupling parameter which varies between 0 and 1; U_i is the potential energy function that represents the initial state; and U_f is the potential energy function that represents the final state.[34] In this linear form of the Kirkwood coupling parameter method, when λ is equivalent to 0 the U_f term tends to 0, thus the system is in the

initial state and is described by the potential function U_i (i.e. CO_2 molecule is in the clathrate).[34] When λ is equivalent to 1 the U_i term tends to 0, therefore the system is in the final state represented by the potential function U_f (i.e. SO_2 molecule is in the clathrate).[34] For any λ values between 0 and 1 the system can be considered in some sort of unphysical intermediate state described by a combination of the U_i and U_f potential functions.[34]

Classical molecular dynamics simulations can utilize the linear Kirkwood coupling parameter method presented in equation 3.7 to evaluate the Gibbs free energy difference at constant pressure with the following equation:[33]

$$U_f(\lambda = 1) - U_i(\lambda = 0) = \Delta G_{reaction} = \int_0^1 \langle \frac{\partial U(\lambda)}{d\lambda} \rangle_{NTp} \partial\lambda \qquad 3.8$$

where $U_f(\lambda = 1)$ is the Gibbs free energy of the final product, and $U_i(\lambda = 0)$ is the Gibbs free energy of the initial reactant.[34] Subtracting the latter two results in the Gibbs free energy difference for the transformation from reactant to product. This equation demonstrates that integrating the ensemble average of the derivative of the potential energy with respect to the coupling parameter yields the Gibbs free energy difference for the transformation of the initial reactant to final product.[34] A series of molecular dynamics simulations using various λ values (between 0 and 1) can be utilized to evaluate the ensemble average $\langle {}^{\partial U(\lambda)}/_{d\lambda} \rangle$.

Using numerous simulations with small λ increments (i.e. 0.05), result in a more accurate evaluation of the integral in equation 3.8. Thus, we can extract more converged free energy differences. Equations 3.7 and 3.8 are the basis for the thermodynamic integration technique for evaluating the difference in Gibbs free energy.

Furthermore, thermodynamic integration (TI) can also be used to evaluate the free energy difference for inserting/deleting a molecule. This is also accomplished by modifying the interaction potential of a molecule. For example, in the creation process, a non-interacting molecule (molecule with no interaction potential) is transformed into an interacting molecule (molecule with an interaction potential). However, when inserting a molecule by means of linear Kirkwood coupling parameter method, one needs extremely small λ increments to properly evaluate the free energy.[34] For example, if you were to insert a molecule (with a full interaction potential) closely to an existing molecule in the system, the interaction between the two would create unphysical forces, resulting in a non-representative evaluation of the free energy.[34] To avoid this problem, the linear method requires numerous simulations (very small λ increments). These small λ values will gradually introduce the interaction potential of the newly added molecule, resulting in realistic forces which lead to a representative evaluation of the free energy.[34]

Unfortunately, using extremely small λ increments makes it expensive to evaluate the change in free energy. Consequently, other solutions to this problem are desirable. Presently, non-linear scaling Kirkwood coupling parameter methods are the most commonly used approach. These methods redesign the linear form of the Kirkwood coupling parameter method (equation 3.7) to the following potential energy function:[34]

$$U(\lambda) = [1 - f(\lambda)]U_i(r^N) + f(\lambda)U_f(r^N) \qquad 3.9$$

where $f(\lambda)$ is a non-linear mixing function which varies continuously between 0 and 1 and satisfies the conditions, $f(0) = 0$ and $f(1) = 1$.[35] Furthermore, these functions should be selected such that, the derivative of $f(\lambda)$ tends to 0 when λ approaches either 0 or 1.[34] If the

function satisfies these conditions, the contribution of the endpoints (λ=0 or λ=1) to the overall free energy integral will diminish, resulting in more converged free energy evaluations.[34] Essentially, these methods put less emphasis on the free energy contribution derived from simulations at the endpoints. For example, the free energy value derived from the λ=0 simulation in the molecule insertion process described earlier, will have less of an impact on the total free energy due to the selective weighing of the non-linear mixing functions. Non-linear mixing functions are used in this work to obtain more converged free energy differences for the substitutions of interest.

Recall, we are interested in evaluating the difference in Gibbs free energy associated with the following transformations using non-linear thermodynamic integration based molecular dynamics simulations:

$$\text{Clathrate}[(n+x)\text{CO2(g)}] + x\text{Y(g)} \rightarrow \text{Clathrate}[n\text{CO2(g)} + x\text{Y}] + x\text{CO2(g)} \quad 3.10$$

where n is the # of CO_2 molecules initially in the clathrate hydrate phase and *x* molecules of gas Y (SO_2, CH_4, H_2S, N_2) at a temperature *T* and pressure *p* replace xCO_2(g) molecules from the structure I clathrate hydrate. The CO_2(g) molecules originally in the clathrate hydrate phase are released into the gas/fluid phase. Using the non-linear Kirkwood coupling method (equation 3.9), MD can evaluate the Gibbs free energy difference associated with the substitution of the gases in the clathrate hydrate phase only.

$$\text{Clathrate}[(n+x)\text{CO}_2\text{(g)}] \rightarrow \text{Clathrate}[n\text{CO}_2\text{(g)} + x\text{Y}] \quad 3.11$$

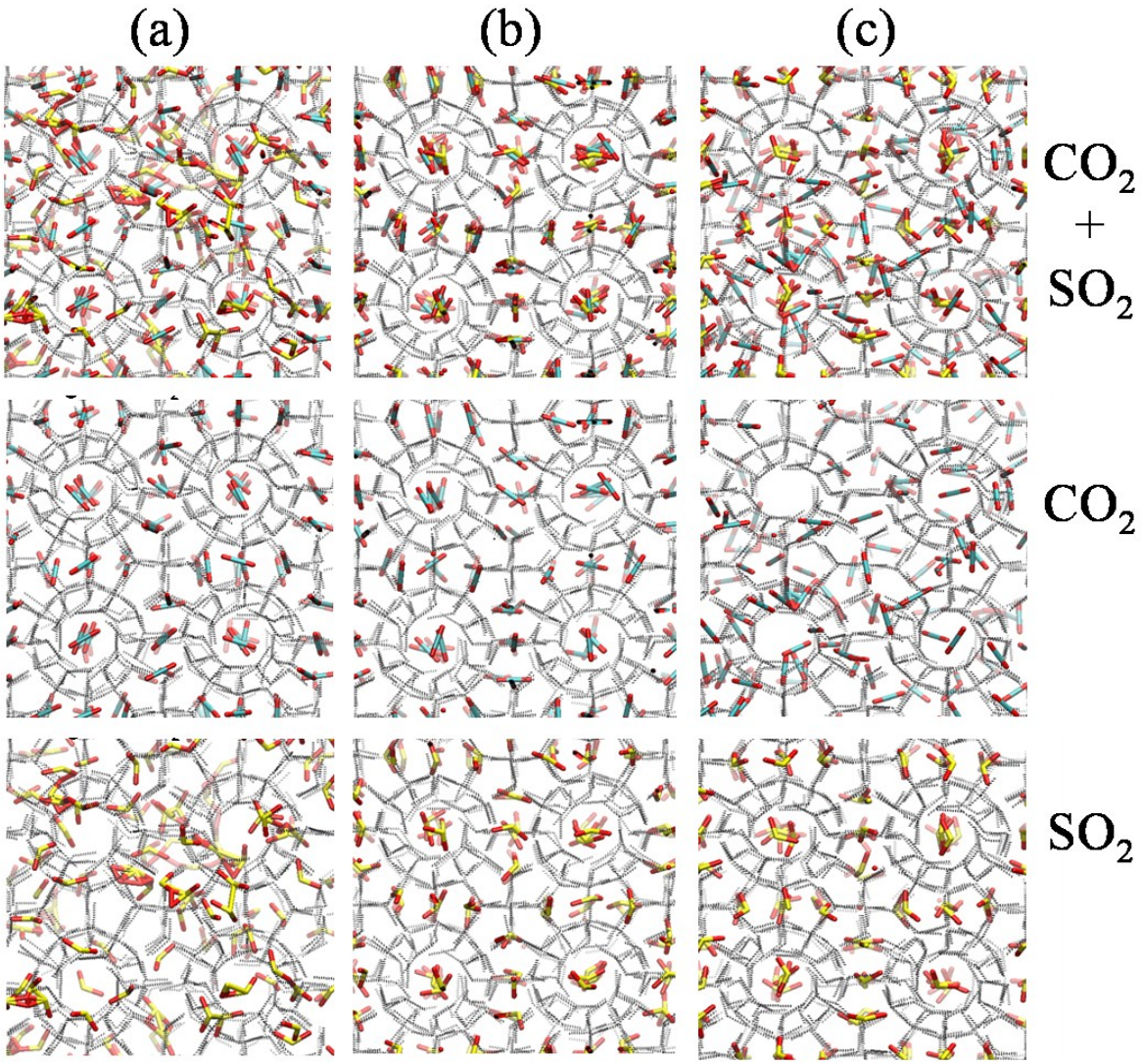

Figure 3.9: Representation of the set-up for the $CO_2 \rightarrow SO_2$ transformation in the thermodynamic integration calculations. a) $\lambda = 0$ shows the CO_2 (green) within the clathrate cages with its full non-bonded potential switched on and SO_2 (yellow) randomly distributed within the clathrate as a ghost atom with no intermolecular potentials. b) $\lambda = 0.5$ shows both CO_2 and SO_2 within the clathrate cages interacting with partial potentials. C) $\lambda = 1$ shows the SO_2 within the clathrate cages with its full non-bonded potential switched on and CO_2 randomly distributed within the clathrate as a ghost atom with no intermolecular potentials.

The coupling constant λ switches off the intermolecular potential energy function for the interactions of the $x CO_2(g)$ guest molecules with the hydrate cage water molecules and

other guests in the simulation. This converts the xCO$_2$(g) molecules to "ghost" molecules which have no interactions potential. Simultaneously, the coupling constant λ switches on the intermolecular potential energy functions of the xY guest molecules which are initially "ghosts" in the simulation cell. Once the transformation is complete, the xY guest molecules will have fully turned on potentials and will be positioned inside the proper clathrate hydrate cages. To illustrate the simulation procedure, the nature of the potential energy functions for the guests at different values of the coupling constant λ is shown in figure 3.9.

The mixing function used in this work to transform the potential energy function from the reactant state (i.e. interacting CO_2 guest in the clathrate) to the product state (i.e. interacting Y guest in the clathrate) is defined by the error function:

$$f(\lambda) = \frac{\alpha}{\sqrt{\pi}} \int_0^{\lambda} \exp\left[-\alpha^2 \left(y - \frac{1}{2}\right)^2\right] dy \qquad 3.12$$

This function is continuous and satisfies the proper boundary conditions at $\lambda = 0$ and $\lambda = 1$. The parameter α is chosen between 10 and 11.[34] Other common non-linear mixing functions were tested such as polynomial mixing function where k is a parameter used to control the behaviour of the mixing function (equation 3.13) and the trigonometric function (equation 3.14):

$$f(\lambda) = 1 - (1 - \lambda)^k \qquad 3.13$$

$$f(\lambda) = \frac{1}{2}\left[1 + \sin\left(\pi\left(\lambda - \frac{1}{2}\right)\right)\right] \qquad 3.14$$

By varying the λ increment (number of simulations), I evaluated the convergence of the free energy change. The error mixing function proved most efficient, as it required fewer simulations (larger λ increment) to obtain converged free energy changes.

As previously mentioned, the free energy difference associated with the transformation shown in equation 3.10 is given by equation 3.8. The derivative of the potential energy function in angular brackets represent the *NpT* ensemble average (average over the course of a simulation performed with constant number of molecules, pressure and temperature) for each value of λ. This is extracted from a number of simulations using small λ intervals and by numerically calculating the value of the Gibbs free energy difference integral. The free energy of this reaction determines whether the CO_2(g) hydrate is thermodynamically stable when the gas Y is present in the flue stream. If the free energy is positive, the substitution is unfavorable and thus the CO_2 clathrate hydrate is more thermodynamically stable. If it is negative the substitution is favorable and the Y clathrate hydrate is more thermodynamically stable. The latter processes may have profound implications on the feasibility of using clathrate hydrates for carbon capture.

Furthermore, when evaluating the change in free energy of the process shown in equation 3.10 using MD, one must also consider the free energy difference resulting from the guest molecule exchange in the gas phase (non-ideality effect). This means that we must also account for the Gibbs free energy change of molecule in the gas phase shown in equation 3.15.

$$x\mathrm{Y(g)} \rightarrow x\mathrm{CO_2(g)} \qquad 3.15$$

For the xCO$_2$(g) molecules in the gas phase at T and p, the Gibbs free energy is:

$$\Delta G_{CO_2}^{gas} = xkTln\left(\frac{\rho_{CO_2}(g;T,p)}{q_{CO_2}}\right) + \mu_{res}[CO_2(g;T,p)] \qquad 3.16$$

where k is the Maxwell-Boltzmann constant, T the temperature, $\rho_{CO_2}(g;T,p)$ is the number density of the CO_2(g) in the gas phase and q_{CO_2} is the ideal gas CO_2(g) partition function. The residual chemical potential for CO_2(g) in the gas phase is determined by the thermodynamic expression:

$$\mu_{res}[CO_2(g;T,p)] = \int_0^p [V(T,p) - V^{IG}(T,p)]dp \qquad 3.17$$

where the real gas molar volume for CO_2(g), $V(p,T)$ can be determined from experimental measurements at T and p, or calculated from MD simulations. The $V^{IG}(p,T)$ term is evaluated as the volume of an ideal gas at pressure p and temperature T of 1 mole of ideal gas using the Ideal Gas Law. Similar expressions can be written for the free energy of the xY guest molecules in the simulation cell.

Combining equation 3.16 and the corresponding relations for the free energies of the Y guest, results in the expression for the free energy difference for the guest molecule exchange in the gas phase (Non-ideal contribution). Adding the free energy difference from the clathrate phase calculated with thermodynamic integration using MD (ΔG_{TI}), provides the total Gibbs free energy difference (ΔG_{TOT}), for the substitution of interest (equation 3.10):

$$\Delta G_{TOT} = xkT\left[ln\left(\frac{\rho_Y(Clathrate;T,p)}{\rho_{CO_2}(Clathrate;T,p)}\right) + ln\left(\frac{\rho_{CO_2}(g;T,p)}{\rho_Y(g;T,p)}\right)\right]$$
$$+x\left[\mu_{res}[CO_2(g;T,p)] - \mu_{res}[Y(g;T,p)]\right] + \Delta G_{TI} \qquad 3.18$$

Given the lack of thermophysical data on some the gases studied in this work, it is not always possible to evaluate ΔG_{TOT}. However, one can simplify the expression for the total Gibbs free energy difference in equation 3.18, by utilizing two approximations. Considering the temperature and pressure conditions relevant for clathrate hydrate formation (273 K and 10 bar), we assume that CO_2(g) and Y(g) behave as ideal gases. This approximation can be

made as temperature and pressure conditions such as these are not enough to induce non-ideal gas behavior. Consequently:

$$\rho_{CO_2}(g;T,p) = \rho_Y(g;T,p) \qquad 3.19$$

$$\mu_{res}[CO_2(g)] = \mu_{res}[Y(g)] = 0 \qquad 3.20$$

Furthermore, the volume difference between different clathrate hydrates (i.e. CO_2 vs SO_2 filled) can be disregarded. This approximation is valid because clathrate hydrates cages are known to be non-compressible, thus there is no change in volume for the inclusion of different guests. Therefore:

$$\rho_{CO_2}(clathrate;T,p) = \rho_Y(clathrate;T,p) \qquad 3.21$$

This reduces the expression of the total Gibbs free energy in equation 3.18 solely to the Gibbs free energy difference extracted from the thermodynamic integration simulations;

$$\Delta G_{TOT} = \Delta G_{TI} \qquad 3.22$$

Using simulation, one can examine the separate contributions of the Van der Waals and electrostatic parts of the intermolecular potential energy to the total Gibbs free energy of CO_2 substitution. Partitioning of the intermolecular interactions into electrostatic and Van der Waals components in the force field will also allow us to partition their contribution to free energy of substitution. The intermolecular interactions of atoms are represented by:

$$U_{non-bonded} = \sum_{i,j} 4\varepsilon_{ij}\left[\left(\frac{\sigma_{ij}}{r_{ij}}\right)^{12} - \left(\frac{\sigma_{ij}}{r_{ij}}\right)^{6}\right] + \sum_{i,j}\frac{q_i q_j}{4\pi\varepsilon_0 r_{ij}} \qquad 3.23$$

where the first term gives the van der Waals contribution and the second term gives the electrostatic contribution to the intermolecular interaction potential. To find the relative contribution of these two terms to the ΔG_{TI} (equation 3.18), we have performed a set of

simulations where the CO_2 guests are substituted with Y guest species without electrostatic point charges:

$$U_{non-bonded} = \sum_{i,j} 4\varepsilon_{ij}\left[\left(\frac{\sigma_{ij}}{r_{ij}}\right)^{12} - \left(\frac{\sigma_{ij}}{r_{ij}}\right)^{6}\right] \qquad 3.24$$

This will allow us to get further insight on the major factors which contribute to clathrate stability and selectivity in hopes of understanding the fundamental factors that influence clathrate hydrate formation potentials in the presence of impurities.

Computational details

Description of model systems

The main objective of this work is to determine the stability of certain clathrate hydrates (i.e. methane, carbon dioxide, nitrogen, hydrogen sulfide and sulfur dioxide) using molecular dynamics simulations. The simulations in this project were performed using the DL_ POLY 2.20 simulation package utilizing the Leap Frog-Verlet algorithms to integrate the equations of motion.[34] They consist of multiple guest gas molecules enclosed in a sI clathrate hydrate.[34] The first step in creating proper sI clathrate hydrate systems ideal for simulations requires the construction of the sI hydrate. This is accomplished by using the water oxygen atom coordinates determined from the sI clathrate X-ray crystal structure.[27] The initial configuration of the water hydrogen atoms were selected according to the TIP4P potential such as to maximize the hydrogen bonding network and minimize the dipole moment of the unit cell.[27] A 3*x*3*x*3 replica of the latter sI clathrate hydrate unit cell containing 6*x*27 = 162 large cages and 2*x*27 = 54 small cages is used. The later sI clathrate water coordinates are positioned in a cubic simulation box with cell vectors (36.00*x*36.00*x*36.00)90° $Å^3$. Periodic boundary conditions were used with 13 Å cutoffs. This distance is less than half the length of the shortest cell vector insuring no self-image interactions. The subsequent step in the creation process, inserts the guest gas molecule of interest (CO_2) at the center of both the large cages and the small cages in the sI clathrate hydrate framework. Rigid potentials were selected for all molecules used in this work. These force fields imply that bonded potentials (bonds lengths, angles etc…) are not represented in the potential energy function describing the intramolecular interactions. Instead the rigid approximations for all molecules are based on extensively developed models able to

accurately represent the bulk thermodynamic properties of interest such as vapor pressure.[27,39-44] The non-bonded potentials (electrostatic and van der Waals) are treated by typical means of Coulombic interactions and Lennard-Jones interactions, respectively.

Finally, any pairwise van der Waals non-bonded interactions including hydrogen atoms were set to 0, otherwise no other constraints were applied. The TIP4P rigid potential was used for water, this potential was selected due to its success in previous work in the Woo lab.[29-31,36,37] The Harris rigid potential was used for CO_2(g), this potential was also selected due to its success in previous work in the Woo lab.[27,31,38] The Ribeiro rigid potential was used for SO_2. This potential is among the most accurate for replicating the vapor pressure without representing the quadrupole moment.[39] The Kamath rigid potential was used for H_2S, this potential was selected due to its capability for reproducing the vapor pressure.[40] In this model the hydrogen atoms do not have any VDW contributions; instead the VDW parameter for the sulfur atom is optimized and chosen to account for the hydrogen atoms. In this way, the model is optimized to accurately represent the hydrogen bonding network of hydrogen sulfide. An anisotropic rigid potential was chosen for N_2. This potential was also selected due to its success in previous work in the Woo lab.[27,41-43] The M parameter represents a charged ghost partical to represent the quadrupole moment of nitrogen. The single point TRAPPE potential was used for CH_4 because it is commonly used and computationally inexpensive.[44] The atomic electrostatic point charges and the Lennard-Jones parameters for the molecules in this work are given in table 3.1.

Table 3.1: Atomic point charges and Lennard-Jones parameters used in this study for the following flue gas impurities H_2O, CO_2, CH_4, SO_2, and H_2S.

Atom	q (e)	σ_{ii} (Å)	ε_{ii} (kcal/mol)
O (H_2O)	0.0000	3.153	0.1550
H (H_2O)	+0.5200	0.000	0.0000
M (H_2O)	-1.0400	0.000	0.0000
C (CO_2)	+0.6512	2.745	0.0595
O (CO_2)	-0.3256	3.017	0.1702
C (CH_4)	0.0000	3.730	0.2941
S (SO_2)	+0.4700	3.585	0.3068
O (SO_2)	-0.2350	2.993	0.1238
S (H_2S)	+0.2520	3.710	0.5524
H (H_2S)	-0.1260	0.000	0.0000
N (N_2)	-0.4954	3.209	0.0809
M (N_2)	+0.9908	0.000	0.0000

Simulation Protocol

Following the initial construction of the clathrate hydrate coordinates as previously described, the geometries were optimized before the themodynamic integration based MD simulations were initiated. One problem with thermodynamic integration simulations is that they require multiple simulations using small λ increments to obtain well converged and continuous free energies. Determining proper balance between accuracy and computational efficiency required some testing. I performed many test sets of thermodynamic integration simulations with different λ increments and evaluated their convergence shown in figure 3.10.

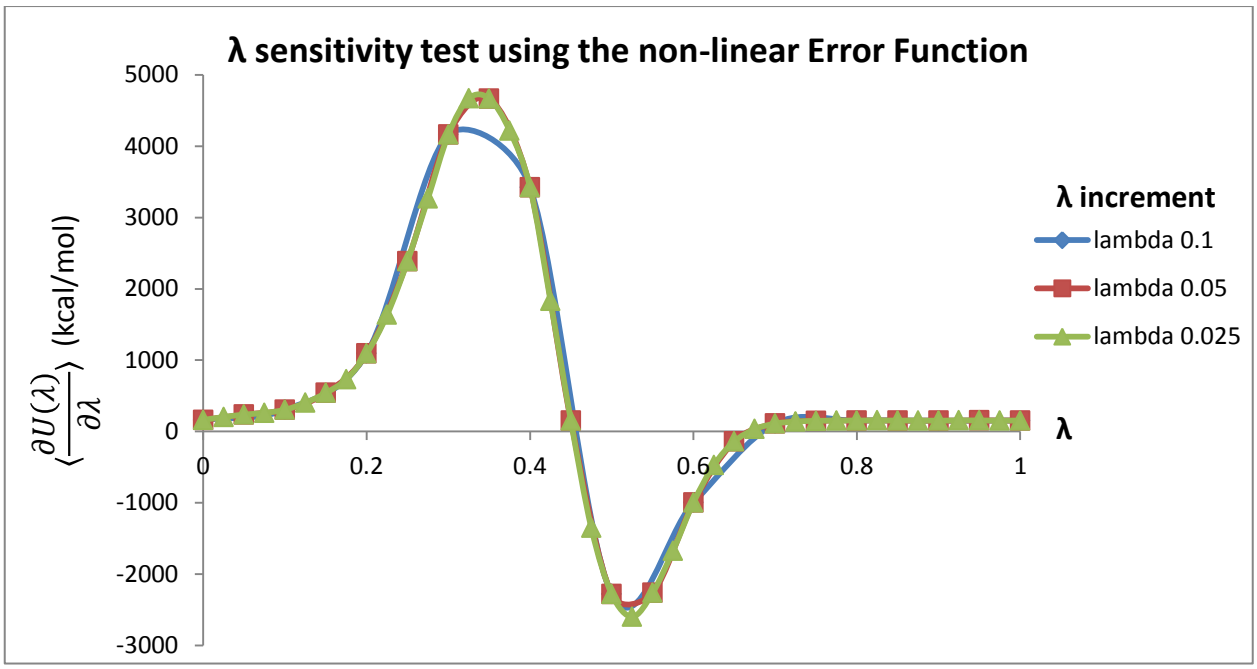

Figure 3.10: Plot representing the free energy convergence of the error function as a function of the λ increment (number of simulations). It is clear that the free energy converges at λ 0.05

It can be observed that the Gibbs free energy can be determined with sufficient accuracy with a λ increment of 0.05. Therefore, 21 total simulations where ideal to perform the transformation of the CO_2 in the clathrate hydrate phase to guest Y (i.e. methane, nitrogen, hydrogen sulfide and sulfur dioxide). In the product CO_2(g), molecules are randomly replaced from both small and large cages with Y guests. Recall, to transform a reactant to a product the λ parameter must be applied to the potential energy functions describing the intermolecular interactions. The replacement fractions of the CO_2(g) guests in the small and large cages in the simulation cell can vary from λ = 0.0 to 1.0 in intervals of 0.05, thus leading to a total of 21 simulations to complete the transformation. Additionally, large cage and small cage substitutions were also performed separately allowing us to further understand the driving force behind the substitutions. Finally, the same procedure was implemented to determine the separate contributions of the Van der Waals and electrostatic

parts of the intermolecular potential energy to the total Gibbs free energy of CO_2 substitution.

The thermodynamic integration method may seem tedious because there are a total of 4 different guests (i.e. CH_4, SO_2, H_2S, and N_2) and total of 5 different types of transformations for each guest (full cage substitution at 200 K, full cage substitution at 273 K, large cage substitution, small cage substitution and partial non-bonded substitution) all requiring 21 simulations to complete the transformation (420 total simulations). However, this work was feasible as I developed a Python program to automate the process for creating appropriate simulations for thermodynamic integration techniques. The program requires minimal supplementary input from the user to generate simulations suitable for free energy calculations using thermodynamic integration based on typical classical molecular dynamics inputs. In general, only three inputs are required for typical DL_POLY simulations; 1) The CONFIG file which contains all the coordinates for the atoms in the system, 2) The FIELD file which contains the force field parameters and 3) the CONTROL file which contains all the simulation parameters and specifications such as temperature, pressure, simulation time etc… The latter files all need to be altered when performing free energy calculations based on thermodynamic integration. My program can perform these changes and submit these simulations using the DL_POLY 2.20 molecular dynamics package with nothing more than the coordinates and atomic types of the Y guest molecule of interest. The program begins by randomly selecting CO_2 molecules located in the CONFIG file in the desired category (all cages, large cages, and small cages) for transformation. The program then creates the coordinates for the Y guests in the appropriate Cartesian space (Y guest is created near the

randomly selected CO_2 guest) and generates the appropriate CONFIG file necessary for free energy calculations based on thermodynamic integration. The program then uses the atomic types provided by the user and a tabulated list of potentials to determine the non-bonded potentials describing the interactions of the newly added Y guest with all of the existing atoms in the simulation calculated using typical Lorentz-Bertholet combination rules:

$$\varepsilon_{ij} = \left(\varepsilon_{ii}\varepsilon_{jj}\right)^{1/2} \qquad 3.25$$

$$\sigma_{ij} = \left(\sigma_{ii}+\sigma_{jj}\right)/2 \qquad 3.26$$

Where the indices i and j represent all the atoms involved in the pairwise interactions, ε represents the well depth of the potential energy describing the Van der Waals interactions at equilibrium, σ represents the finite distance between the pairwise interactions for all atoms where the Van der Waals interaction energy is zero. The program then generates the necessary FIELD file suitable for free energy simulations based on thermodynamic integration. Finally, the program also modifies the CONTROL file appropriately. More specifically, the program analyzes the previously created input files and generates a new CONTROL file with the necessary free energy initiation specifications such as the reactant and product atoms, lambda value and other parameters necessary for proper thermodynamic integration procedure. Once all the newly created input files are complete, they are submitted with the lambda value 0 to 1 in increments of 0.05 creating the aforementioned 21 simulations required to complete a transformation. These simulations can all run simultaneously.

Simulations were all performed using the DL_POLY 2.20 molecular dynamics program[34] in the *NpT* ensemble with Nosé/Hoover thermostat and barostat constants of 0.2

and 0.5 ps, respectively. The temperature and pressure of the simulations were 200 K and 1 bar. In addition, simulations were also performed at 273 K to observe the effect of temperature on the free energy of substitution. Simulations were carried out for 500 ps with the first 100 ps used for equilibration with a timestep of 1 fs to integrate the equations of motion. All simulations used the SHAKE algorithm for rigid molecule motion. The Ewald summation method was used to treat Coulombic interactions and all intermolecular interactions in the simulation box were calculated within a cutoff distance of 13 Å.

Results and Discussion

Structure I clathrate hydrates have been suggested as carbon dioxide capture/separation tools for flue stream derived from coal combustion plants. Understanding the disruption potential of common gas impurities found in the flue stream at conditions relevant for hydrate formation (273 K and 10 bar) is imperative for determining the feasibility of this method. Our goal is to evaluate the relative thermodynamic stability of each sI clathrate hydrate (i.e. CH_4, CO_2, N_2, SO_2, and H_2S) using Gibbs free energy calculations based on thermodynamic integration via MD simulations. These substitution thermodynamics will be evaluated for three different substitutions: the full substitutions in all cages, the substitutions in the large cages only and finally the substitution in the small cages only. The effect of temperature on the substitution process will also be investigated. Finally, by partitioning the non-bonded potential into separate contributions (i.e. Van der Waals and electrostatics) we hope to acquire further insight on the driving force behind the substitution process.

Recall, there are two components to the substitution process, the guest substitution in the clathrate phase (calculated from simulation) and the guest substitution in the gas phase (calculated using the non-ideality component). Simulations provide the free energy for the guest substitution in the clathrate phase. These simulations were performed at a temperature of 273 K and 1 bar of pressure. Since the clathrate is non-compressible, this is a good approximation for conditions relevant for hydrate formation (10 bar). An example of the integrand in equation 3.8 is shown in figure 3.11 where all CO_2 guests in the sI clathrate are replaced by SO_2 guests (substitution in equation 3.33).

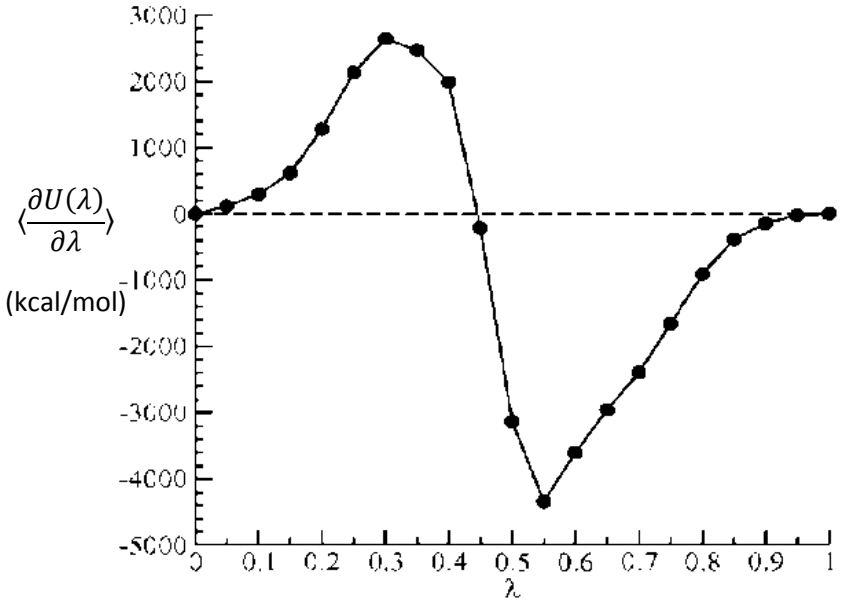

Figure 3.11: A representation of the $\langle {}^{\partial U(\lambda)}/_{\partial \lambda} \rangle$ for different values of λ for the $CO_2 \rightarrow SO_2$ substitution in the clathrate hydrate. The integration of this curve gives ΔG_{TI}.

Initially, at λ=0 the Gibbs free energy is positive thus unfavorable (CO_2-cage interactions are dominant). As λ varies from 0 to 0.5 (weakening of the CO_2–cage interactions and strengthening the SO_2–cage interactions), the free energy change tends to more negative values. This suggests that the SO_2-cage interactions are more favorable than the CO_2-cage interactions. Moreover, once λ>0.5, the Gibbs free energy change becomes favorable, this is a result of the SO_2-cage interactions becoming more dominant than the less favored CO_2-cage interactions. Evaluating the area under the curve in figure 3.11 provides ΔG_{TI} for the substitution in equation 3.31.

`

a. CO_2 *substitution with* CH_4

The Gibbs free energy of the carbon dioxide guest substitutions with methane in the sI clathrate hydrate cages are given in table 3.2. In the first set of simulations, all CO_2 guests in the sI clathrate hydrate are substituted by CH_4 guests at 273 K and 10 bar (equation 3.27).

$$Clathrate[8CO_2(S+L)] + 8CH_{4(g)} \rightarrow Clathrate[8CH_4(S+L)] + 8CO_{2(g)} \quad 3.27$$

Table 3.2: Gibbs free energy per guest substitution of CO_2(clathrate) → CH_4(clathrate) in the sI clathrate hydrate at 273 K 10 bar. The Non-ideal gas contributions are calculated at conditions relevant for hydrate formation (273 K and 10 bar). Van der Waals and electrostatic contributions to the total Gibbs free energy are also presented.

Substitution	ΔG_{TOT} (kcal/mol)	ΔG_{TI} (kcal/mol)	$\Delta G_{Non\text{-}ideality}$ (kcal/mol)	$\Delta G_{TI\ (VdW)}$ (kcal/mol)	$\Delta G_{TI\ (Elec.)}$ (kcal/mol)
All cages	-0.39	-0.38	-7.1×10^{-3}	-0.38	-
Large cages	-	-0.39	-	-	-
Small cages	-	-1.54	-	-	-

The total Gibbs free energy for the substitution in equation 3.27 is –0.39 kcal/mol for each guest. This value includes the non-ideality effects of the molecule exchange in the gas phase ($-7.1\text{x}10^{-3}$ kcal/mol). These results demonstrate that methane sI clathrate hydrates are more stable than CO_2 sI clathrate hydrates at 273 K and 10 bar. Further dissection of the free energy reveals the separate contributions of the small and large cages. The Gibbs free energy for the substitution of CO_2 with CH_4 in the large cages only (equation 3.28) is -0.39 kcal/mol per guest.

$$Clathrate[8CO_2(S+L)] + 6CH_{4(g)} \rightarrow Clathrate[6CH_4(L) + 2CO_2(S)] + 6CO_{2(g)} \quad 3.28$$

Furthermore, the substitution of CO_2 with methane in the small cages only (equation 3.29) is −1.54 kcal/mol per guest.

$$Clathrate[8CO_2(S+L)] + 2CH_{4(g)} \rightarrow Clathrate[6CO_2(L) + 2CH_4(S)] + 2CO_{2(g)} \quad 3.29$$

These values show that the carbon dioxide gas in both the large and small cages of CO_2 sI clathrate hydrates are thermodynamically susceptible to substitution with CH_4. Unfortunately, these favorable Gibbs free energy differences suggest that if a significant amount of uncombusted methane is present in the flue stream, it may spontaneously replace CO_2 in both the small and large cages. Although the bulk of the CO_2 capacity (large cages) will remain unsubstituted the 2:6 small cage/large cage ratio of sI clathrate hydrate indicates that methane can considerably impede efficient carbon capture. This suggests that CO_2 capture using sI clathrate hydrates will not likely be feasible at 273 K and 10 bar.

In addition, partitioning the cage substitutions into large and small cages allow us to evaluate the effect of binary hydrates. These effects will demonstrate the influence of a binary CO_2/CH_4 sI clathrate hydrate on the thermodynamics stability of $CO_2 \rightarrow CH_4$ substitutions. Table 3.2 summarizes our results. Results in table 3.2 suggest that the most stable phase of the sI clathrate hydrate occurs when the small cages are substituted with methane and the large cages are occupied by CO_2 (largely negative ΔG for small cage substitutions). These small cage substitutions are ideal in terms of using binary clathrates as hydrate promoters, as they will not hinder the bulk of the CO_2 uptake capacity. Promoters are suggested for reducing the conditions (temperature and pressure) necessary to form the hydrates. However, the large cage substitution can also be favored; this is problematic in the carbon capture application because the large cages represent the bulk to the CO_2 uptake

capacity. Thus its consideration as a hydrate promoter at these conditions (273 K and 10 bar) should be questioned.

The united atom TRAPPE potential was chosen to represent CH_4. Our simulations were able to study the separate contributions of the Van der Waals and the electrostatics to the Gibbs free energy of substitutions. This methane potential would suggest that the favourability of the $CO_2 \rightarrow CH_4$ substitutions is related to the effective radius of methane. Table 3.6 demonstrates that the Van der Waals radius of methane is much smaller than that of CO_2, this can make it easier to accommodate in the cages resulting in a favorable ΔG_{VDW} (negative ΔG_{VDW} given in table 3.2). However, further dissection of the separate contributions is not possible as this model does not utilize charges to describe methane behavior. Instead, it uses only the Van der Waals interactions to represent methane interactions. In order to make any conclusions, the effect of the non-bonded potential of methane on the ΔG_{TOT} should be investigated.

b. CO_2 *substitution with* N_2

The Gibbs free energy of the carbon dioxide guest substitutions with nitrogen in the sI clathrate hydrate cages are given in table 3.3. In the first set of simulations, all CO_2 guests in the sI clathrate hydrate are substituted by N_2 guests at 273 K and 10 bar (equation 3.30).

$$Clathrate[8CO_2(S+L)] + 8N_{2(g)} \rightarrow Clathrate[8N_2(S+L)] + 8CO_{2(g)} \qquad 3.30$$

Table 3.3: Gibbs free energy per guest substitution of CO_2(clathrate) → N_2(clathrate) in the sI clathrate hydrate at 273 K 10 bar. The Non-ideal gas contributions are calculated at conditions relevant for hydrate formation (273 K and 10 bar). Van der Waals and electrostatic contributions to the total Gibbs free energy are also presented.

Substitution	ΔG_{TOT} (kcal/mol)	ΔG_{TI} (kcal/mol)	$\Delta G_{Non\text{-}ideality}$ (kcal/mol)	$\Delta G_{TI\ (VdW)}$ (kcal/mol)	$\Delta G_{TI\ (Elec.)}$ (kcal/mol)
All cages	1.37	1.36	-9.7×10^{-3}	0.33	1.03
Large cages	-	1.59	-	-	-
Small cages	-	-0.20	-	-	-

The total Gibbs free energy for the substitution in equation 3.30 is 1.37 kcal/mol for each guest. This value includes the non-ideality effects of the molecule exchange in the gas phase ($-9.7\text{x}10^{-3}$ kcal/mol). These results demonstrate that carbon dioxide sI clathrate hydrates are more stable than nitrogen sI clathrate hydrates. This behavior is to be expected, as sI nitrogen clathrate hydrates do not form at conditions of 273 K and 10 atm. As a result this gas cannot be considered as a hydrate promoter. Further dissection of the free energy reveals the separate contributions of the small and large cages. The Gibbs free energy for the substitution of CO_2 with N_2 in the large cages only (equation 3.31) is 1.59 kcal/mol per guest.

$$Clathrate[8CO_2(S+L)] + 6N_{2(g)} \rightarrow Clathrate[6N_2(L) + 2CO_2(S)] + 6CO_{2(g)} \qquad 3.31$$

Additionally, the substitution of CO_2 with N_2 in the small cages only (equation 3.32) is –0.20 kcal/mol per guest.

$$Clathrate[8CO_2(S+L)] + 2N_{2(g)} \rightarrow Clathrate[6CO_2(L) + 2N_2(S)] + 2CO_{2(g)} \qquad 3.32$$

These values show that the carbon dioxide gas in the large cages of CO_2 sI clathrate hydrates are not thermodynamically susceptible to substitution with N_2. However, the Gibbs free energy for the substitution of carbon dioxide gas in the small cages of CO_2 sI clathrate

hydrates show that CO_2 in the small cages are thermodynamically susceptible to substitution with N_2. These results indicate that the most stable form of the sI clathrate hydrate would be a binary CO_2/N_2 hydrate phase, where CO_2 is in the large cages and N_2 in the small cages. Unfortunately, due to the high concentration of nitrogen in the atmosphere and in the combustion gas, CO_2 capture using sI clathrate hydrates could be severely hampered by the formation of N_2 clathrates at 273 K and 10 bar. Although the bulk of the cages (large cages) in CO_2 sI clathrate hydrates are not susceptible to substitution with N_2, the small cages of CO_2 sI clathrate hydrates can be substituted. Since the small cage/large cage ratio of sI clathrate hydrate is 2:6, this suggests that 25% of the CO_2 capacity can be substituted resulting in a drastic decrease in carbon capture efficiency. As a result, sI clathrate hydrates could consume large amounts of energy to capture N_2 (a harmless gas) from flue stacks. This could have serious implications for CO_2 capture by clathrate hydrates. It is important to note that these simulations only investigate the thermodynamics of substitution. Kinetics of N_2 substitution in the small cages of sI clathrate hydrate is also important.

Separate contributions of the N_2 non-bonded potential were also analyzed in hopes of gaining a better understanding of the small vs large cage selectivity. These values are given in table 3.3 and show that the electrostatic contribution to the ΔG_{TI} is larger than the Van der Waals contribution (1.03 and 0.33 kcal/mol, respectively). From the values given in table 3.6, we can see that the Van der Waals radius of N_2 is significantly smaller than CO_2. This would make this guest easier to accommodate in the small sI clathrate hydrate cages. This should result in a smaller contribution of the ΔG_{VdW} to the positive ΔG_{TI} (shown in table 3.3). Furthermore, the large positive $\Delta G_{Elec.}$ suggests that N_2 is disfavored in the large cages due to

its electrostatics. This could be a result of the smaller quadrupole moment of N_2 compared to the larger more favorable quadrupole moment of CO_2. The effect of multipole moments should be further investigated before determining the fundamental reason for selectivity.

Table 3.4: The molar volumes of CO_2, CH_4, and N_2 (m^3/mol) at 200 K for different pressures (bar) and the residual contribution to the Gibbs free energy from each gas (kcal/mol). [d] at 273 K

Gas	Pressure (bar)	$V_m(p,T)$ (m^3/mol)	$V_m^{ig}(p,T)$ (m^3/mol)	$V_m(p,T)-V_m^{ig}(p,T)$ (m^3/mol)	$\mu_{res}[X(g;T,p)]$
CO_2[45]	0.5	0.032940	0.033260	-3.2×10^{-4}	
	1	0.016312	0.016628	-3.2×10^{-4}	-2.40×10^{-4}
	1.01325	0.016094	0.016411	-3.2×10^{-4}	
	10 [f]	0.002081	0.002245	-1.6×10^{-4}	-1.55×10^{-4}
CH_4[46]	0.1	0.16617	0.16628	-1.1×10^{-4}	
	0.5	0.033156	0.033256	-1.0×10^{-4}	
	1	0.016523	0.016628	-1.0×10^{-4}	-1.04×10^{-4}
	1.01325	0.016305	0.016411	-1.0×10^{-4}	
	10 [d]	0.002189	0.002245	-5.5×10^{-5}	-5.53×10^{-4}
N_2[47]	0.2	0.083126	0.083145	-1.9×10^{-5}	
	0.4	0.041528	0.041572	-4.4×10^{-5}	
	0.6	0.027678	0.027715	-3.7×10^{-5}	
	0.8	0.0207512	0.020786	-3.5×10^{-5}	
	1	0.016593	0.016629	-3.6×10^{-5}	-3.11×10^{-5}
	1.01325	0.016375	0.016411	-3.7×10^{-5}	
	10 [d]	0.002234	0.002245	-1.1×10^{-5}	-1.09×10^{-4}

Table 3.5: Simulation cell volumes (Å^3) for each clathrate at 200K and 1 bar.

	V(clathrate; T,p)	$\ln\left(\frac{\rho_Y(clathrate;T,p)}{\rho_{CO_2}(clathrate;T,p)}\right)$
Clathrate(CO_2)	44877	-
Clathrate(SO_2)	45475	-0.013
Clathrate(H_2S)	44376	0.011
Clathrate(CH_4)	44671	0.005
Clathrate(N_2)	44581	-0.007

Table 3.6: The van der Waals radii (Å) and polarity of the guest species Y studied in this work.

Y	van der Waals radius (Å) [a]	Electrostatic moment
SO_2	3.98	μ = 1.62 D [b]
CO_2	3.85	$\Theta = -4.3\times10^{-26}$ statC·cm^2 [c]
H_2S	3.12	μ = 0.97 D [d]
CH_4	2.98	N/A [e]
N_2	2.65	$\Theta = -1.4\times10^{-26}$ statC·cm^2 [c]

[a] Ref.[48,49] [b] Ref.[39] [c] Ref.[50] [d] Ref.[40]

[e] No electrostatic charge is used in the united atom TRAPPE potential for CH_4.

c. CO_2 *substitution with* SO_2

The Gibbs free energy of the carbon dioxide guest substitutions with sulfur dioxide in the sI clathrate hydrate cages are given in table 3.7. Unfortunately, the necessary thermophysical data for SO_2 (and H_2S) is not available to calculate the $\Delta G_{non\text{-}ideal}$ component of the ΔG_{TOT} in the same manner as was determined for CH_4 and N_2 using the first and second term in equation 3.18 and the data presented in tables 3.4 and 3.5. However, at these pressures (10 bar) we note that these non-ideal corrections for nitrogen and methane are on the orders of 10^{-3} kcal/mol and account for less than 2% of the ΔG_{TOT} (refer to table 3.2 and 3.3). Therefore, $\Delta G_{non\text{-}ideal}$ is approximated to be zero in the calculation of the ΔG_{TOT} for SO_2 and H_2S. This approximation can be further justified by considering the gases as ideal

(equation 3.19 and 3.20) and by considering the clathrate hydrates as non-compressible (equation 3.21).

In the first set of simulations, all CO_2 guests in the sI clathrate hydrate are substituted by SO_2 guests at 273 K and 10 bar (equation 3.33).

$$Clathrate[8CO_2(S+L)] + 8SO_{2(g)} \rightarrow Clathrate[8SO_2(S+L)] + 8CO_{2(g)} \quad 3.33$$

Table 3.7: Gibbs free energy per guest substitution of CO_2(clathrate) → SO_2(clathrate) in the sI clathrate hydrate at 273 K 10 bar. Van der Waals and electrostatic contributions to the total Gibbs free energy are also presented.

Substitution	ΔG_{TOT} (kcal/mol)	$\Delta G_{TI\ (VdW)}$ (kcal/mol)	$\Delta G_{TI\ (Elec.)}$ (kcal/mol)
All cages	-1.63	-0.99	-0.91
Large cages	-2.05	-	-
Small cages	-0.63	-	-

The total Gibbs free energy for the substitution in equation 3.33 is –1.63 kcal/mol for each guest. These results demonstrate that SO_2 sI clathrate hydrates are more stable than CO_2 sI clathrate hydrates. Further examination of the free energy reveals the separate contributions of the small and large cages. The Gibbs free energy for the substitution of CO_2 with SO_2 in the large cages only (equation 3.34) is -2.05 kcal/mol per guest.

$$Clathrate[8CO_2(S+L)] + 6SO_{2(g)} \rightarrow Clathrate[6SO_2(L) + 2CO_2(S)] + 6CO_{2(g)} \quad 3.34$$

The substitution of CO_2 with SO_2 in the small cages only (equation 3.35) is –0.63 kcal/mol per guest.

$$Clathrate[8CO_2(S+L)] + 2SO_{2(g)} \rightarrow Clathrate[6CO_2(L) + 2SO_2(S)] + 2CO_{2(g)} \quad 3.35$$

These values show that the carbon dioxide gas in both the large and small cages of CO_2 sI clathrate hydrates are thermodynamically susceptible to substitution with sulfur dioxide. Furthermore, these favorable Gibbs free energy differences suggest that if SO_2 is present in sufficient quantities in the flue stream, CO_2 capture using sI clathrate hydrates may not be feasible at 273 K and 10 bar. Fortunately, current desulfurization technologies are very mature and wide spread.[54]

CO_2/SO_2 binary sI clathrate hydrates were also studied. These effects are shown in table 3.7. When evaluating the Gibbs free energy for substituting the large cages only (equation 3.34), it is clear that having a binary CO_2/SO_2 sI clathrate hydrate, with CO_2 is in the small cages and SO_2 in the large cages will be the most stable phase for this hydrate. This computational prediction is in agreement with experimental studies which show that the phase boundary for the CO_2/SO_2 binary sI clathrate hydrate is found at lower pressures and temperatures compared to the CO_2 sI hydrate (refer to figure 3.4).[18,51] Unfortunately, this gas favors the large cages and forms clathrates more readily than CO_2, thus this gas should not be investigated as a hydrate promoter, as it will impede the bulk of the CO_2 capture. Therefore, this impurity would need to be removed further from the flue stream prior to CO_2 capture.

The contribution of the Van der Waals and electrostatic potentials to the Gibbs free energy for the $CO_2 \rightarrow SO_2$ transformation are shown in table 3.7. These values are almost equal at –0.99 and –0.91 kcal/mol, respectively. Both contributions have a negative Gibbs free energy implying that SO_2 is the thermodynamically favored guests over CO_2 from both the van der Waals guest – water and electrostatic guest-water interactions. Let us examine

the van der Waals radius and electrostatic moment of SO_2 given in table 3.6 to further understand SO_2 selectivity.[39,40,48-50,52] Van der Waals radii values show that SO_2 is larger than CO_2, therefore there must be another underlying reason that SO_2 is favored in both small and large cages in terms of ΔG_{VdW}. Table 3.6 also demonstrates the electrostatic moment of SO_2 is considerably larger than any other guests. However, further investigation is required to understand the favorable nature of the ΔG_{VdW} and $\Delta G_{Elec.}$ before the underlying reason can be conclusively determined.

d. CO_2 *substitution with* H_2S

The Gibbs free energy of the carbon dioxide guest substitutions with hydrogen sulfide in the sI clathrate hydrate cages are given in table 3.8. In the first set of simulations, all CO_2 guests in the sI clathrate hydrate are substituted by H_2S guests at 273 K and 10 bar (equation 3.36).

$$Clathrate[8CO_2(S+L)] + 8H_2S_{(g)} \rightarrow Clathrate[8H_2S(S+L)] + 8CO_{2(g)} \quad 3.36$$

Table 3.8: Gibbs free energy per guest substitution of CO_2(clathrate) → H_2S(clathrate) in the sI clathrate hydrate at 273 K 10 bar. Van der Waals and electrostatic contributions to the total Gibbs free energy are also presented.

Substitution	ΔG_{TOT} (kcal/mol)	$\Delta G_{TI\ (VdW)}$ (kcal/mol)	$\Delta G_{TI\ (Elec.)}$ (kcal/mol)
All cages	-1.55	-1.30	-0.26
Large cages	-1.12	-	-
Small cages	-2.73	-	-

The total Gibbs free energy for the substitution in equation 3.36 is –1.55 kcal/mol for each guest. These results demonstrate that H_2S sI clathrate hydrates are more stable than CO_2 sI clathrate hydrates. Further dissection of the free energy reveals the separate contributions

of the small and large cages. The Gibbs free energy for the substitution of CO_2 with H_2S in the large cages only (equation 3.37) is -1.12 kcal/mol per guest.

$$Clathrate[8CO_2(S+L)] + 6H_2S_{(g)} \rightarrow Clathrate[6H_2S(L) + 2CO_2(S)] + 6CO_{2(g)} \quad 3.37$$

Furthermore, the substitution of CO_2 with SO_2 in the small cages only (equation 3.37) is

–2.73 kcal/mol per guest.

$$Clathrate[8CO_2(S+L)] + 2H_2S_{(g)} \rightarrow Clathrate[6CO_2(L) + 2H_2S(S)] + 2CO_{2(g)} \quad 3.38$$

These values show that the carbon dioxide gas in both the large and small cages of CO_2 sI clathrate hydrates are thermodynamically susceptible to substitution with hydrogen sulfide. Unfortunately, these favorable Gibbs free energy differences suggest that if H_2S is present in the flue stream, CO_2 capture using sI clathrate hydrates will not likely be feasible at 273 K and 10 bar. Similar to the case of SO_2, if H_2S is present in sufficient quantities it can considerably impede efficient carbon dioxide capture. Fortunately, due to the toxicity of hydrogen sulfide and its high concentration in "sour gas", combustion plants today are equipped with technologies for removing this contaminant before it is released into the atmosphere.[54]

CO_2/H_2S binary sI clathrate hydrates were also studied. These effects are shown in table 3.8. Contrary to SO_2, the free energy values presented in table 3.8 suggest that a binary CO_2/H_2S sI clathrate hydrate, with CO_2 is in the large cages and H_2S in the small cages will be the most stable phase for this hydrate. Unlike SO_2, little is known of the clathrate hydrate formation potential of H_2S and further investigation of this gas' clathrate hydrate formation potential is necessary before conclusion can be made on the its efficacy to hinder clathrate

hydrate CO_2 uptake.[53] If the hydrate formation potential of H_2S coincides with the conditions necessary for carbon capture using clathrate hydrates, it too could have the capability of obstructing CO_2 capture. This would result in the necessary removal of the H_2S impurity from the flue stream prior to CO_2 capture. However, as previously mentioned the most stable phase for these clathrates contain CO_2 in the large cages and H_2S in the small cages. This type of binary hydrate is an ideal candidate in the hydrate promotion application. If hydrogen sulfide clathrates require milder conditions, the possibility of using this gas as a promoter exists. Unfortunately, large cage substitutions are also still favored this will likely further discredit the use of sI clathate hydrates as carbon capture tools.

Similarly, Van der Waals and electrostatic contributions to the ΔG_{TI} were evaluated. According to the results in table 3.8 the ΔG_{VdW} is much larger than the electrostatic contribution (–1.30 and –0.26 kcal/mol per guest, respectively). Referring to table 3.6, we can observe that the Van der Waals radius of H_2S is significantly smaller than CO_2 which makes it easier to accommodate into the sI clathrate hydrate cages. This could account for the Van der Waals stabilization effect to the Gibbs free energy. Furthermore, the smaller magnitude of the dipole moment of the H_2S guests compared to SO_2 can be attributed to the smaller magnitude of the electrostatic contributions for ΔG_{TI} for this guest. Nonetheless, the small dipole moment of H_2S leads to favorable contributions of the electrostatic potential to free energies of substitution of CO_2. The effects of the separate components of the non-bonded potential should be further investigated before determining the fundamental reasons for selectivity.

e. Effect of temperature on the Gibbs free energy of substitution

Since the free energies of substitution evaluated at 273 K do not bode well for CO_2 capture with clathrate hydrates, we examined the free energies of substitution at a lower temperature (200K). This should give us some indication of the effect of temperature on the Gibbs free energy for CO_2 substitutions with flue gas impurities. Our results are summarized in table 3.9.

Table 3.9: Gibbs free energy per guest substitution of CO_2(clathrate) → Y(clathrate) in the sI clathrate hydrate at 273 K and 200 K at 10 bar.

Y	**Substitution**	ΔG_{TOT} **(273 K) kcal/mol**	ΔG_{TOT} **(200 K) kcal/mol**
SO_2	**All cages**	-1.63	-1.90
	Large cages	-2.05	-2.30
	Small cages	-0.63	-0.77
CH_4	**All cages**	-0.38	-0.13
	Large cages	-0.39	0.35
	Small cages	-1.54	-1.26
H_2S	**All cages**	-1.55	-1.56
	Large cages	-1.12	-0.82
	Small cages	-2.73	-2.76
N_2	**All cages**	1.11	1.36
	Large cages	1.53	1.59
	Small cages	-0.20	-0.37

In all simulations with SO_2, H_2S, and N_2, the value of the ΔG_{TI} per guest molecule at 200 K varied by less than 0.3 kcal/mol per substitution relative to the values at 273 K. The SO_2 and H_2S hydrates become slightly more thermodynamically stable at the 200 K relative to CO_2 clathrates in all substitution reactions, with the exception of the H_2S large cage substitutions. Unfortunately, the effect of temperature in these cases further hinders the CO_2 uptake and the feasibility of using sI clathrate hydrates as carbon capture tools. On the other hand, N_2 substitutions are only further stabilized in the small cages; otherwise the

substitutions in the large cages are further destabilized. It is clear that the effect of temperature does not change the thermodynamics of substitution for SO_2, H_2S and N_2 in terms of CCS application. However, in the case of CH_4 hydrates the substitution thermodynamics in the large cages become significantly less stable at 200 K. We can observe this by comparing the Gibbs free energy difference at 273 K and 200K (-0.39 kcal/mol per guest vs 0.35 kcal/mol per guest, respectively). This makes the CO_2 guests in the large cages of sI clathrate hydrate unsusceptible to substitutions. Consequently, the decrease in temperature can have a profound impact on the feasibility of using sI hydrates for carbon capture. Because CH_4 is favored only in the small cages, it has potential to be used as a hydrate promoter. Meaning it may be able to reduce the conditions of hydrate formation, making it easier to form CO_2 clathrates in a binary CO_2/CH_4 mixture. Furthermore, the large cage substitutions are now disfavored, this renders in the bulk of the CO_2 capacity (large cages) unsusceptible to substitutions. These nonspontaneous substitutions make binary CO_2/CH_4 hydrates prime candidates for hydrate promotion. Additionally, because CH_4 favors the replacement of CO_2 in the small cages, it will have minimal impact on the CO_2 uptake capacity of the hydrate (2:6 small cage/large cage ratio). However, uncombusted methane is not very concentrated in the flue stream, thus the use of CH_4 as a promoter should be investigated further to determine if the reduction of the conditions (temperature and pressure) for hydrate formation outweighs the compromise in CO_2 uptake capacity. These studies would indicate that having a binary CO_2/CH_4 hydrate would be economically feasible compared to the pure CO_2 hydrates. Furthermore, substituting CO_2 in the small cages may not have a negative effect in terms of capture. Since CH_4 is a much more potent (21 times) greenhouse gas than CO_2, it is also desirable to remove this flue gas impurity from the

atmosphere. The binary CO_2/CH_4 hydrates should be further investigated in the application of carbon capture.

Results from a previous study by the Woo Lab on methane substitution with CO_2 from the sI clathrate hydrate under deep ocean pressures and temperatures near 273 K,[27] are in agreement with this work. The Woo lab found that CO_2 is favored in the large sI cages, and CH_4 is favored in the small sI clathrate hydrate cages. The relative magnitude of the Gibbs free energy for substitution of CO_2 with CH_4 in the small and large cages is different in this work and Ref. [27] and this can be related to the different thermodynamic conditions of the two sets of simulations or the different intermolecular potential used for methane in Ref. [27]. Although the results are considerably different, the same trends can be drawn and used to conclude that a binary mixture of CO_2/CH_4 is the most stable clathrate hydrate that can form at the given temperatures and conditions.

Another previous study performed by the Woo lab was used to determine the methane storage capacity in the structure H clathrate hydrate under high pressure conditions.[30,31] In those studies, it was observed that the calculated values of the Gibbs free energy for methane encapsulation from the gas phase show strong sensitivity to the intermolecular potential energy function used for methane. This must be taken into account when interpreting the numerical values of the Gibbs free energy of CO_2 substitution with CH_4.

Conclusions

Molecular dynamics simulations were used to evaluate the free energy of substituting CO_2 in clathrate hydrates by N_2,CH_4, SO_2 and H_2S flue gas impurities under conditions proposed for CO_2 capture (273 K, 10 bar). Under these conditions, structure I CO_2 clathrate hydrates that have both small and large cages in a 2:6 ratio are known to form. In this work, our goal was to examine how thermodynamically susceptible CO_2 sI clathrates were to substitution by N_2,CH_4, SO_2 and H_2S in both the large and small cages.

For post-combustion CO_2 capture, nitrogen is an important gas to consider for substitution as it is present in high concentrations within the combustion flue gas. Although N_2 clathrate hydrates do not form at these temperature and pressure conditions, our simulations suggested that CO_2 sI clathrates may be susceptible to substitution by N_2 only in the small cages. More specifically, we found that CO_2 substitution by N_2 in the small sI cages was thermodynamically favorable by 0.20 kcal/mol per guest substitution. This substitution is problematic in terms of efficient CO_2 capture because a significant amount of energy is spent on forming the N_2 clathrates. Since the small cages make up 25% of the sI clathrate cages, a significant amount of energy could be spent on removing N_2 from the flue gas rather than CO_2. It is important to note that these simulations only evaluate the thermodynamics of the substitution process, not the kinetics of the process. So if the substitution is slow, the presence of N_2 may not be problematic for CO_2 capture using clathrate hydrates. Unfortunately, previous experimental studies of methane clathrates under similar conditions (Park et al. *Proc. Natl. Acad. Sci. U.S.A.* **2006,** *103*, 12690) revealed that N_2 can rapidly substitute CH_4 in the sI clathrates. The kinetics of CO_2 sI calthrate substitution by N_2 is not expected to be significantly different, however further experimental study of this issue is necessary to confirm this assertion.

The thermodynamics of CO_2 substitution by SO_2 and H_2S in sI clathrate hydrates was also examined. In both cases, the substitution was highly favored in the full cage substitution process (1.63 and 1.55 kcal/mol for SO2 and H2S, respectively). Moreover, substitution of CO_2 by these gases in both the small and large cages was determined to be favorable. This suggests that these gases may also disrupt the CO_2 capture by sI clathrate hydrates if they are present in large concentrations in the combustion flue stream. However, since these gases are not typically present in high concentration due to desulfurization technologies, they should not present a problem for post-combustion CO_2 scrubbing. Unfortunately, SO_2 and H_2S gases can be present in relatively high concentration in natural gas from so-called unconventional reservoirs (reservoirs not usually fit or selected for natural gas extraction due to their contamination). Presently, there are increasing amounts of natural gases being extracted from unconventional reservoirs such as shale gas due to the shortage of conventional (ideal) reservoirs. As a result, there is an interest in CO_2 scrubbing technologies for natural gas purification. These reservoirs typically have high levels of CO_2 (~15%), where clathrate hydrates could be used for CO_2 removal in pre-combustion purification. Since SO_2 and H_2S need to be removed from natural gas, our results suggest that a sI clathrate hydrate based technology (at conditions of 200K and 10 bar) could be used for removal of all three gases.

Finally, the thermodynamics of CO_2 substitution by methane in sI clathrate hydrates was examined. Substitution in both the small and large cages was calculated to be favorable, although substitution in the small cages was significantly more exergonic with ΔG_{TOT} being -1.54 and -0.39 kcal/mol for small and large case substitutions, respectively. Since methane is a 21 times stronger greenhouse gas than CO_2, its concomitant removal during post-combustion CO_2 scrubbing is desirable. On the other hand, for natural gas purification, these

results suggest that a sI clathrate hydrate based technology could not be used since CO_2 scrubbing would be disrupted by methane, the primary component of natural gas.

Because the results at 273 K and 10 bar were not particularly promising for CO_2 capture by sI clathrate hydrates, we evaluated the same substitution thermodynamics at 200 K and 10 bar. This was done to determine if CO_2 sI calthrate hydrates were less susceptible to substitution at lower temperatures. With one exception, we found that the substitution free energies change by less than 0.3 kcal/mol, and do not alter the sign of free energies. Thus, using a lower capture temperature does not significantly change the substitution free energies and their implications for CO_2 capture by sI clathrate hydrates. The only exception to this was the substitution of CO_2 by CH_4 in the large cages. The calculated substitution free energy changed from ΔG_{TOT}= -0.39 kcal/mol at 273 K to +0.35 kcal/mol at 200 K. This might make it more feasible for using sI clathrate hydrates for natural gas purification, however further analysis and experimentation would be required as lower temperature processes are energetically costly.

The total free energies of substitution were also broken down into non-ideal gas effects, Van der Waals and electrostatic contributions to the substitution process. At the pressures proposed for CO_2 capture (~10 bar) using sI clathrate hydrates, non-ideal gas effects were found to be negligible and can be neglected for other gases under similar conditions. The substitution free energies were also dissected into the individual contributions of the non-bonded potential energy function (Van der Waals and electrostatics) to evaluate their effect on the total Gibbs free energy of substitution between CO_2 and flue gas impurities in sI clathrate hydrates. It is clear that these contributing factors strongly

depend on the species of interest. However, it can be observed that the size of the guest plays a major role in the substitution process. Further studies are required before accurate conclusions can be made on the electrostatic contributions to the total Gibbs free energy of substitution.

As part of this work, the free energy calculations were automated. In these calculations, thermodynamic integration is performed where the CO_2 molecules in the sI clathrate hydrate cages are incrementally mutated into the substituting gases N_2, SO_2, H_2S or CH_4. These simulations are tedious and are prone to human error because numerous steps are involved in the setup of the molecular dynamics input files needed at each stage. Thus, significant effort was put into fully automating the procedure, such that the user only needs to create input files containing the atomic types and coordinates of the initial and final gases. The program was capable of fully automating the procedure of creating all of the intermediate input files, submitting the jobs, and integrating the free energy changes. Moreover, the program was written in a way that it is not limited to the specific application of clathrate hydrates. For example, it could be used to mutate a functional group within a metal organic framework to examine the change in adsorption free energies. This will greatly simplify and accelerate any future mutational free energy calculations done in the Woo lab.

(1) Morgan, M. G.; Cantor, R.; Clark, W. C.; Fisher, A.; Jacoby, H. D.; Janetos, A. C.; Kinzig, A. P.; Melillo, J.; Street, R. B.; Wilbanks, T. J. *Environmental Science & Technology* 2005, *39*, 9023-9032.

(2) Nations, U. *http://www.ipcc.ch/SPM2feb07.pdf* 2007.

(3) Nations, U. *http://www.unfccc.int/resource/docs/convkp/conveng.pdf* 1992.

(4) Nations, U. *http://www.unfccc.int/resource/docs/convkp/kpeng.pdf* 1998.

(5) Aaron, D.; Tsouris, C. *Separation Science and Technology* 2005, *40*, 321-348.

(6) Klara, S. M.; Srivastava, R. D. *Environmental Progress* 2002, *21*, 247-253.

(7) Oi, L. E. *SIMS2007 Conference* 2007, *Telemark Univeristy College*.

(8) Herzog, H. M., J.; Hatton, A. *Clean air task force* 2009.

(9) Banerjee, R.; Phan, A.; Wang, B.; Knobler, C.; Furukawa, H.; O'Keeffe, M.; Yaghi, O. M. *Science* 2008, *319*, 939-943.

(10) Vaidhyanathan, R.; Iremonger, S. S.; Shimizu, G. K. H.; Boyd, P. G.; Alavi, S.; Woo, T. K. *Science* 2010, *330*, 650-653.

(11) Haines, J.; Cambon, O.; Levelut, C.; Santoro, M.; Gorelli, F.; Garbarino, G. *Journal of the American Chemical Society* 2010, *132*, 8860-+.

(12) Han, S. S.; Choi, S. H.; van Duin, A. C. T. *Chemical Communications* 2010, *46*, 5713-5715.

(13) Adeyemo, A.; Kumar, R.; Linga, P.; Ripmeester, J.; Englezos, P. *International Journal of Greenhouse Gas Control* 2010, *4*, 478-485.

(14) Linga, P.; Kumar, R.; Lee, J. D.; Ripmeester, J.; Englezos, P. *International Journal of Greenhouse Gas Control* 2010, *4*, 630-637.

(15) Sloan, E. D. *Journal of Chemical Thermodynamics* 2003, *35*, 41-53.

(16) Petrucci, R. H. H., F.G.; Madura, J.D.; Bissonnette, C. *Pearson* 2011, *10*, 214,560.

(17) Linga, P.; Kumar, R.; Englezos, P. *Journal of Hazardous Materials* 2007, *149*, 625-629.

(18) Beeskow-Strauch, B.; Schicks, J. M.; Spangenberg, E.; Erzinger, J. *Chemistry-a European Journal* 2011, *17*, 4376-4384.

(19) Stevens, S. H.; Kuuskraa, V. A.; Gale, J. In *Greenhouse Gas Control Technologies*; C S I R O: East Melbourne, 2001, p 278-283.

(20) Stevens, S. H. K., V. A.; Gale, J.; Beecy, D. *Envir. Geosciences* 2001, *8*, 200-209.

(21) House, K. Z.; Schrag, D. P.; Harvey, C. F.; Lackner, K. S. *Proceedings of the National Academy of Sciences of the United States of America* 2006, *103*, 12291-12295.

(22) Côté, M. M. W., J. F. *SPE*, *DOI: 10.2118/138121-MS*.

(23) Uddin, M.; Coombe, D.; Law, D.; Gunter, B. *Journal of Energy Resources Technology-Transactions of the Asme* 2008, *130*, 14.

(24) Uddin, M.; Coombe, D.; Wright, F. *Journal of Energy Resources Technology-Transactions of the Asme* 2008, *130*, 11.

(25) Wright, J. F. C., M. M.; Dallimore S. R. *Proced. 6th Inter. Conf. Gas Hydrates* 2008, *Vancouver, BC, Canada*.

(26) Englezos, P. *Industrial & Engineering Chemistry Research* 1993, *32*, 1251-1274.

(27) Dornan, P.; Alavi, S.; Woo, T. K. *Journal of Chemical Physics* 2007, *127*, 8.

(28) Susilo, R.; Alavi, S.; Ripmeester, J.; Englezos, P. *Fluid Phase Equilibria* 2008, *263*, 6-17.

(29) Alavi, S.; Ripmeester, J. A.; Klug, D. D. *Journal of Chemical Physics* 2006, *125*, 10.

(30) Alavi, S.; Ripmeester, J. A.; Klug, D. D. *Journal of Chemical Physics* 2007, *126*, 6.

(31) Alavi, S.; Woo, T. K. *Journal of Chemical Physics* 2007, *126*, 7.

(32) Haryanto, A.; Hong, K. S. *Computers & Chemical Engineering* 2011, *35*, 25-40.

(33) Leach, A. R. *Prentice Hall* 1996.

(34) Smith, W. F., T.R.; Todorov, I.T. *Version 2.20* 2009.

(35) Steinbrecher, T.; Mobley, D. L.; Case, D. A. *The Journal of chemical physics* 2007, *127*, 214108.

(36) Abascal, J. L. F.; Sanz, E.; Fernandez, R. G.; Vega, C. *Journal of Chemical Physics* 2005, *122*, 9.

(37) Alavi, S.; Ripmeester, J. A.; Klug, D. D. *Journal of Chemical Physics* 2006, *124*,

(38) Harris, J. G.; Yung, K. H. *Journal of Physical Chemistry* 1995, *99*, 12021-12024.

(39) Ribeiro, M. C. C. *Journal of Physical Chemistry B* 2006, *110*, 8789-8797.

(40) Kamath, G.; Lubna, N.; Potoff, J. J. *Journal of Chemical Physics* 2005, *123*, 7.

(41) van Klaveren, E. P.; Michels, J. P. J.; Schouten, J. A.; Klug, D. D.; Tse, J. S. *Journal of Chemical Physics* 2001, *115*, 10500-10508.

(42) van Klaveren, E. P.; Michels, J. P. J.; Schouten, J. A.; Klug, D. D.; Tse, J. S. *Journal of Chemical Physics* 2001, *114*, 5745-5754.

(43) van Klaveren, E. P.; Michels, J. P. J.; Schouten, J. A.; Klug, D. D.; Tse, J. S. *Journal of Chemical Physics* 2002, *117*, 6637-6645.

(44) Martin, M. G.; Siepmann, J. I. *Journal of Physical Chemistry B* 1998, *102*, 2569-2577.

(45) Span, R.; Wagner, W. *Journal of Physical and Chemical Reference Data* 1996, *25*, 1509-1596.

(46) Younglove, B. A.; Ely, J. F. *Journal of Physical and Chemical Reference Data* 1987, *16*, 577-798.

(47) Jacobsen, R. T.; Stewart, R. B.; Jahangiri, M. *Journal of Physical and Chemical Reference Data* 1986, *15*, 735-909.

(48) Davidson, D. W.; Handa, Y. P.; Ratcliffe, C. I.; Ripmeester, J. A.; Tse, J. S.; Dahn, J. R.; Lee, F.; Calvert, L. D. *Molecular Crystals and Liquid Crystals* 1986, *141*, 141-149.

(49) Davidson, D. W.; Handa, Y. P.; Ratcliffe, C. I.; Tse, J. S.; Powell, B. M. *Nature* 1984, *311*, 142-143.

(50) Bondi, A. *Journal of Physical Chemistry* 1964, *68*, 441-&.

(51) Cady, G. H. *Journal of Physical Chemistry* 1983, *87*, 4437-4441.

(52) Buckingh.Ad; Disch, R. L.; Dunmur, D. A. *Journal of the American Chemical Society* 1968, *90*, 3104-&.

(53) Mohammadi, A. H.; Richon, D. *Journal of Chemical and Engineering Data* 2009, *54*, 2338-2340.

(54) Biondo, S.J.; Marten,J.C., *Journal of the Air Pollution Control Association*, 1977, 27, 948–961.

Chapter 4: Future investigations and applications

Conclusions

In this thesis, two distinct projects were explored using molecular dynamics simulations. The first project involved novel cryoprotectants called antifreeze glycoproteins (AFGPs) and some of their respective analogues. The compounds are composed of a repeating (Ala-Ala-Thr) polypeptide backbone and linked to a variety of carbohydrates. Ben and coworkers have recently experimentally developed a metric called the hydration index, which correlates well to the cryogenic performance of these compounds. The hydration index is composed of two fundamental properties, the partial molar volume and the hydration number of the solute in water. The goal of the first project was to examine if molecular dynamics simulations could be used to calculate the hydration index to potentially screen for new AFGP analogues before significant effort is put into their synthesis. To calculate the volumetric properties from molecular dynamics, the density of the solutions was averaged from MD simulations. Using a variety of approaches, it was determined that these properties could not be calculated with sufficient accuracy to yield predictive results for the research and development of novel cryoprotectants.

The second project involved the use of novel carbon capture materials to mitigate anthropogenic CO_2 release into the atmosphere. Under specific conditions (273 K and 10 bar) water is known to form ordered crystalline cages around non-polar molecules called clathrate hydrates. Recently, it has been suggested that clathrates could be used for scrubbing CO_2 from coal combustion gases. (Coal combustion is responsible for approximately 40% of the World's anthropogenic CO_2 emissions.) Understanding the influence of flue gas impurities derived from coal combustion on the CO_2 sI clathrate hydrate formation process is

imperative to investigate the feasibility of using these materials. In this thesis, molecular dynamics simulations are combined with transmutation based thermodynamic integration methods to examine the relative free energies of CO_2 clathrate hydrates compared to N_2, CH_4, SO_2 and H_2S. If there is a strong thermodynamic driving force to form clathrate hydrates with gases other than CO_2, this may disrupt the CO_2 capture process or minimally make it less efficient. However, if CO_2 clathrate hydrates preferentially form over other gases, such as N_2, then this could be used as a means of removing CO_2 from combustion gases for subsequent permanent storage. Overall, our results were not encouraging for CO_2 capture by clathrate hydrates. Most problematically, it was found that it is favourable for N_2 to substitute CO_2 in the small cages of the sI clathrate hydrate phase. This is problematic as the small cages make up 25% of the guest sites in sI clathrates meaning that significant amount of energy would put into removing N_2 from the flue stream. This is expected to dramatically reduce the efficiency of the CO_2 capture process. The substitution thermodynamics of SO_2, H_2S and CH_4 were also explored at 273K and 10 atm, where the free energies of replacing CO_2 by these three gases in both the small and large cages would found to be favourable. If these gases are present in large concentrations in the combustion gas, then they could potentially disrupt the CO_2 capture. However, since they are typically not present in large concentration in the combustion gas, and since they are either toxic or stronger greenhouse gases than CO_2, these results suggest that this approach could be used to remove these unwanted gases from the flue stream. Finally, we explored the temperature dependence of the substitution free energies by performing the simulations at 200 K. Except for methane substitution in the small cages, the calculated results at lower temperature were not significantly different compared to 273K. Moreover, the implications for post-combustion CO_2 capture did not change.

Overall, the calculated substitution free energies suggest that using clathrate hydrates for post-combustion CO_2 scrubbing will have significant challenges as binary mixtures of N_2/CO_2 clathrate hydrates are thermodynamically favoured over pure CO_2 clathrates. We note that we have only examined the thermodynamics of the substitution process and that the kinetics of the substitution can be important. However, previous experimental studies suggest that the substitution process in clathrates is rapid.

Future Work

Currently, classical MD studies in the literature are limited to exploring hydroxyl-hydroxyl hydrogen bonding, polypeptide backbone-carbohydrate distances, and configurational folding in hopes of discovering the fundamental reason for potent IRI activity. However, these methods have not yet proven successful making novel approaches desirable.

One such method is the QSAR (qualitative structure-activity relation) approach. This method is likely to be a more efficient for screening novel AFGPs for potent IRI activity. QSAR analyzes simple structural features of the compounds to predict the activity of a certain property. Although QSAR technology seems promising, heavy parameterization is required on small test sets of AFGPs before the tool cab become predictive. In this case, a known library of current native AFGPs and AFGP analogues would be required as a training set for the QSAR method. This library will teach the program what structural features in the compounds are common for potent IRI activity. The program then learns to seek out key structural features in the novel analogues to determine their ice recrystallization inhibition potency. Once the training set is large enough, this method should become extremely

powerful at predicting IRI activity in the novel AFGP analogues; Making QSAR research a long term exploration.

In this work, classical molecular dynamics simulations were used to determine the disruption potential of flue gas impurities on the carbon capture potential of sI clathrate hydrate. These simulations were performed using the rigid potential approximation. Although the latter is a good approximation due to the non-compressible nature of the clathrate hydrates, it would be desirable to replicate the simulations in this work considering the bonded interactions (variable bond lengths, angles). Moreover, this work mentions the possibility of using gases such as methane as a clathrate hydrate promoter. This can lead to reduced formation conditions for CO_2 clahrate hydrates in binary mixture of CH_4/CO_2. The practicality of cases such as these should be investigated to determine if it is more economically feasible to trade-off CO_2 uptake capacity in the clathrate hydrate for lowered pressure and higher temperature conditions.

A further application of this work can be for the purification of natural gas from shale gas. Shale gas has substantially greater amounts of CO_2 than other gases; the present calculations give a basis for studying gas hydrate formation as a means of purifying the resulting shale gas mixture.

Finally, I developed a program that utilizes typical classical molecular dynamics input and creates inputs suitable for free energy calculations. Due to the increasing amounts of attention for the use of MOFs as carbon capture materials, it would be desirable to apply the same program and procedure in this work to metal organic frameworks to gain further insight on the disruption potential of impurities in flue gas in carbon capture. In addition, my

program can also help evaluate separate non-bonded (electrostatics and van der Waals) contributions to the Gibbs free energy. This can lead to further insight on the driving force behind selectivity and uptake of these materials.